5-11-2013

PbZrTiO3 and BiFeO3 Ferroelectric Domains, Domain Boundaries, and Switching Investigated with Piezo Force Microscopy

Linghan Ye
Institute of Materials Science, linghan.ye@uconn.edu

$PbZrTiO_3$ and $BiFeO_3$ Ferroelectric Domains, Domain Boundaries, and Switching Investigated with Piezo Force Microscopy

Linghan Ye

B.S., Beijing University of Technology, 2010

A Thesis

Submitted in Partial Fulfillment of the

Requirements for the Degree of

Master of Science

At the

University of Connecticut

2013

APPROVAL PAGE

Masters of Science Thesis

$PbZrTiO_3$ and $BiFeO_3$ Ferroelectric Domains, Domain Boundaries, and Switching Investigated with Piezo Force Microscopy

Presented by

Linghan Ye, B.S.

Major Advisor_____
Bryan D. Huey

Associate Advisor_____
George A. Rossetti, Jr

Associate Advisor_____
Ramamurthy Ramprasad

University of Connecticut

2013

Acknowledgements

First, I would like to thank my advisor Dr. Bryan D. Huey for his great encouragement and guidance throughout the whole work and also for his understanding and support through hard times. I would also like to thank Huey Nano measuremnt Lab members: James Louis Bosse, Dr. Varun Vyas, Vincent Palumbo, Yasemin Kutes, Alejandro Lluberes, Joshua Leveillee, Manuel Rivas, Alexandra Merkouriou and former group member Dr. Nicholas Polomoff for their help and support in my efforts and creating a friendly work environment.

I would also like to thank the workers at Asylum Research for providing readily available technical support for the AFM.

And I would like to thank those professors and students that provide sample to us and collaborations.

Finally, I would like to thank my family in China for the love and support they send from thousands of miles away.

List of Figures

Table of Contents

Abstract

The domain structure of ferroelectric and multiferroic materials can have a significant effect on piezoelectric, dielectric, and thermal transport properties. Piezo Force Microscopy is an ideal tool based on Atomic Force Microscopy that allows unique investigations of such nanoscale effects, and can further be implemented to monitor domain switching dynamics.

A new method for polarization orientation mapping and statistical analysis is first employed to determine the domain variants present in a range of $BiFeO_3$ epitaxial (001) thin films with specifically engineered domain distributions. This allows domain wall densities to also be calculated, along with interfacial polarization angles between adjacent domains (ferroelectric 180°, and ferroelectric and/or ferroelastic 109° and 71° interfaces). Domain walls can be identified as charged or un-charged as well, which interestingly is identified for the first time as depending on the horizontal or vertical alignment of the domain boundary. For certain domain engineered specimens, particularly those with only 2 domain variants present, this leads to charged interfaces exclusively along <100> and neutral interfaces along <010>, therefore providing a route for unique, direction dependent future ferroelectric or multiferroic devices. Furthermore, increased domain wall densities are shown for the first time to inversely correlate with thermal conductivity, suggesting that domain walls scatter phonons similar to grain boundaries. Again, this can be used to engineer unique transport properties for future ferroelectric and multiferroic devices.

The domain polarization process itself is also investigated using PFM. For epitaxial (001) $PbZrTiO_3$, movies of consecutive domain maps are acquired during the switching process itself. Analysis of domain wall positions as a function of poling time therefore reveals domain growth velocities, which are determined in a variety of directions. Results are presented

based on a range of prepoled domain patterns, designed to isolate domain wall velocities as a function of crystallographic directions as well as possible AFM scanning artifacts. Experimental artifact effects are in fact negated, with domain growth enhanced perpendicular to the AFM fast scanning axis regardless of the crystallographic alignment. Initial domain patterning conditions are found to influence domain growth, however, likely suggesting charge depletion or accumulation in the PZT film adjacent to pre-poled structures. Such insight is crucial for ferroelectric domain engineering efforts and the ultimate performance of ferroelectric devices.

Chapter 1. Background

1.1 Ferroelectricity

Ferroelectric materials have attracted tremendous attention in the last fifty years since they have numerous applications in electronics such as nonvolatile random access memory (FRAM) devices for high-density data storage. Ferroelectric materials have a spontaneous electric polarization that can be reversed by an electric field[1], revealing thermodynamically switchable polarization properties[2]. There is a corresponding hysteresis loop in the polarization versus electric field which can be leveraged for data storage. FRAM thus has the same functionality as the widely employed flash memory, but is one of the most promising future technologies due to its lower power usage and higher writing speed [3].

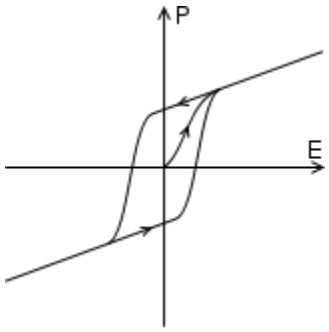

Figure 1.1 typical Ferroelctric polarization hysteresis loop[2].

The crystal system can be divided into 32 crystal classes. 20 of them lack a center of symmetry and exhibit electrical polar properties, i.e. piezoelectricity. Materials with ferroelectricity have 2 or more identical orientation states at zero electric field. At the Curie point Tc, there is a phase transition. Above this temperature, the ferroelectric

materials change to the prototype phase which has the highest symmetries, dPs/dT is negative, and the spontaneous polarization disappears [4]. A variety of materials have been found to exhibit ferroelectricity. For example, Rochelle salts have several upper and lower Curie temperatures that make them ferroelectric and non-ferroelectric; Potassium dihydrogen phosphate only has a single Curie temperature; and Barium titanate has two transitions between absolute zero and the Curie temperature because the crystal can be ferroelectric in two or more directions [5].

We focus on perovskites with the composition ABO_3, where A and B are usually pairs of metals and transition metals [6]. In the ferroelectric state, the center ion is slightly displaced from the center of the unit cell. This generates a dipole moment, which when exposed to an electric field causes linear electromechanical interactions, i.e. the unit cell lattice is extended or compressed by the applied external electric field.

In response to a mechanical stress, piezoelectric materials also can accumulate charge. It can be understood as an electromechanical interaction and a reversal process. Since Ferroelectrics have D is the electric charge displacement, ε is the permittivity, and E is the electric field strength [7]. An applied d-c field E causes an enhanced locally acting field E' by the polarization P it creates:

$$\mathbf{E'=E} + \boldsymbol{\omega}\frac{\boldsymbol{P}}{\boldsymbol{\varepsilon_0}}; \qquad (1)$$

where $\omega=\frac{1}{3}$, the Lorentz factor. The polarization P (dipole moment per unit volume) is measured macroscopically by the electric susceptibility χ, which is the difference between the static and optical dielectric constants. Microscopically this is caused by the

polarizability $\alpha$of N molecular entities per unit volume under the influence of a locally acting field E':

$$\mathbf{P}=\chi\varepsilon_0\mathbf{E}=\mathbf{N}\alpha E'; \quad (2)$$

$$\chi = \kappa_s' - \kappa_i'; \quad (3)$$

Polarization is also related to the temperature:

$$\mathbf{N}\alpha = \frac{C}{T}; \text{ [4]} \quad (4)$$

1.2 AFM

Atomic Force Microscopy (AFM) is a type of microscopy with spatial resolution on the order of nanometers. AFM employs a sharp tip to scan on the sample surface. When the tip is approaching the surface, van der Waals forces (attractive and repulsive), capillary forces, and electromagnetic forces can all be involved. Generally, this perturbs the cantilever to which the AFM tip is attached, which is measured using a laser spot reflected into segmented photodiodes. Recording these signals while scanning the probe in x, y, or z forms an image of the topography or other properties being detected. The primary modes of operation for AFM are Contact mode and AC mode.

Contact mode

In this operation mode, the AFM tip is brought in contact with the sample surface, and the repulsive force between them is kept constant during scanning by maintaining a constant deflection. This is achieved with a feedback loop that is constantly trying to maintain a constant deflection at a set point value by extending or contracting the Z scanner at any given X-Y coordinate. Any necessary changes in the Z actuation thus define the topography [8]. When the spring constant of the cantilever is less than the

surface, the tip bends exactly proportional according to the change in height. For more compliant specimens (not employed here), the measured displacement is always smaller than actual height changes since the specimen will deform in addition to the lever deflecting. An important advantage of contact mode operation is that it enables particularly fast scanning, especially useful for friction imaging, studying dynamics, etc. An obvious disadvantage is that the lateral forces applied while scanning in contact may deform soft samples, cause permanent sample or tip damage, or require a relatively large contact area. All of these circumstances can worsen image resolution[9].

Figure 1.2 Tip in contact mode.

Intermittent mode (Tapping)

In this mode, the cantilever is vibrated at its resonant frequency, usually with a small diether piezoactuator built into the tip holder (distinct from the x, y, and z piezos that scan the surface). The oscillation amplitude is typically around 20-100nm, at frequencies ranging from 5 to 500 kHz. While scanning, the tip is thus tapping the surface many times per location. A height image can now be obtained by tracking the z-actuation necessary to keep a constant oscillation amplitude (instead of deflection), using a similar feedback loop as with contact mode imaging. A phase image can also be recorded in tapping mode. When the tip touches the sample at the bottom of its swing (or in fact is exposed to any force or force gradient), the phase of oscillation is disturbed, inducing a phase difference between the tip and the oscillator that is driving it. The contrast of a phase image is thus loosely dependent on the elastic properties of the sample [9], though

more complicated versions can also extract electronic, magnetic, thermal, or other properties.

The main advantages for AC or tapping modes are higher resolution imaging of samples (and with tips) that are easily damaged, primarily because lower loads are employed, and/or lateral loads are effectively eliminated. On the other hand, disadvantages for AC modes are that they necessitate lower speed imaging and more extensive hardware.

Figure 1.3 Tip in the tapping mode.

1.3 Piezo Force Microscopy (PFM)

Piezo Force Microscopy (PFM) employs a conductive AFM probe to measure the local electromechanical response when a sample is exposed to an electric field, showing in 5. The specimen can also be biased (before, or during) by the conductive probe, which for ferroelectrics can be useful for pre-poling certain domain patterns.

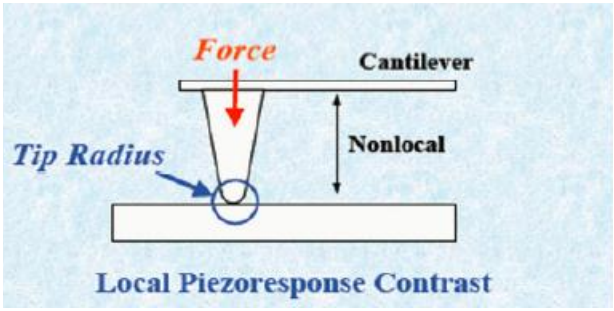

Figure 1.4 PFM measurement[11].

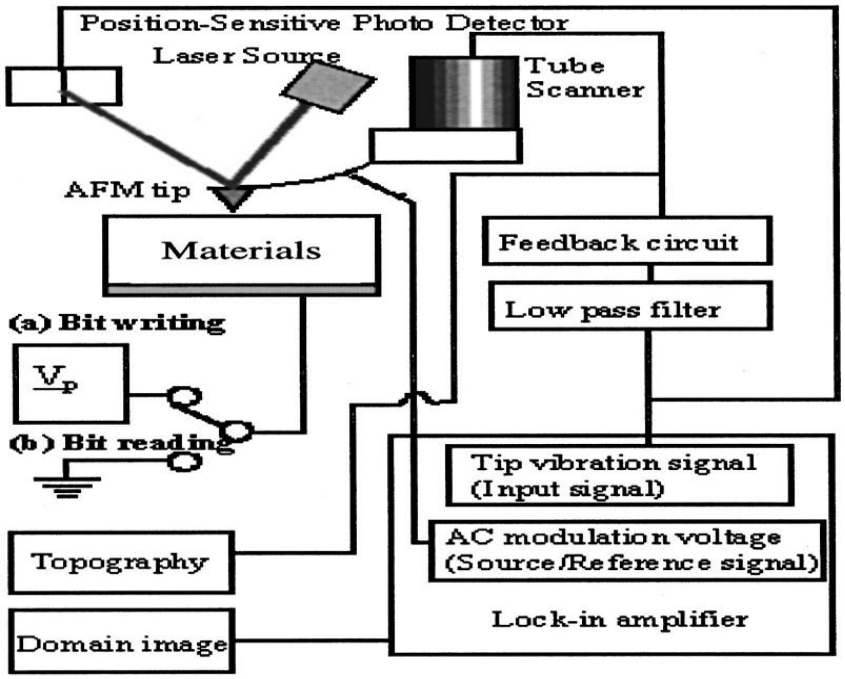

Figure 1.5 PFM setup.

There are three components in a typical PFM system: AFM, Lock-in Amplifier and Function Generator. A Function generator is external electronic equipment used to generate different types of electrical waveforms such as sine waves, triangle waves and saw tooth shapes. It can do so for superimposed or individual frequencies from Hz to MHz, enabling frequency sweeps that are often beneficial in PFM measurements. It can also include AC and DC components, and is typically connected directly to the tip and sample during PFM measurements.

A Lock-in amplifier is a high sensitivity external unit that extracts a signal at a certain frequency from a noisy environment and determines the amplitude and phase. Technically, it takes the input signal, eliminates any frequency components other than the frequency of interest (typically locked onto some external source), amplifies the recovered signal, and compares it to a reference wave (often a synchronization channel from the function generator)[10].

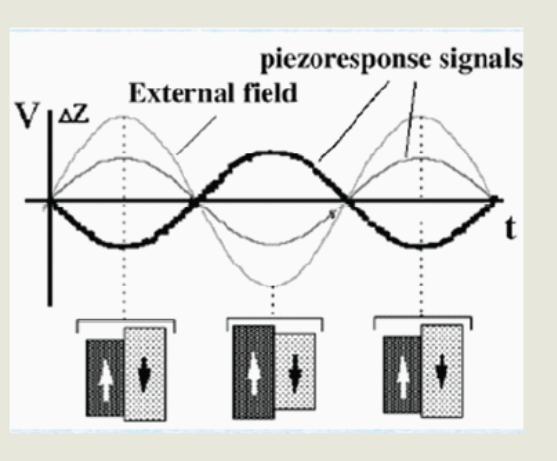

Figure 1.6 PFM response signal[11].

With PFM one can correlate the microstructure and ferroelectric domain polarizations simultaneously, as the PFM electromechanical actuation occurs at a relatively high frequency (usually 500 kHz to 2 MHz), while the AFM topography is essentially a DC measurement of the tip position (averaging out the very small scale piezoactuations). The direction of sample polarization beneath the AFM tip defines the phase response as described in Figure 1. 6. If the polarization is parallel with an applied electric field, the piezo effect will be positive for a positive voltage, and the sample will locally expand. If the polarization is anti-parallel, the sample will shrink due to the reversed piezo effect. When applying an ac field, oppositely oriented domains with respect to the applied field thereby exhibit 180 degree phase shifts.

Piezo effect

The amplitude image acquired in PFM represents the magnitude of the piezoelectric signal, while the phase image gives detail about the polarization orientation, showing in Figure 1. 7.

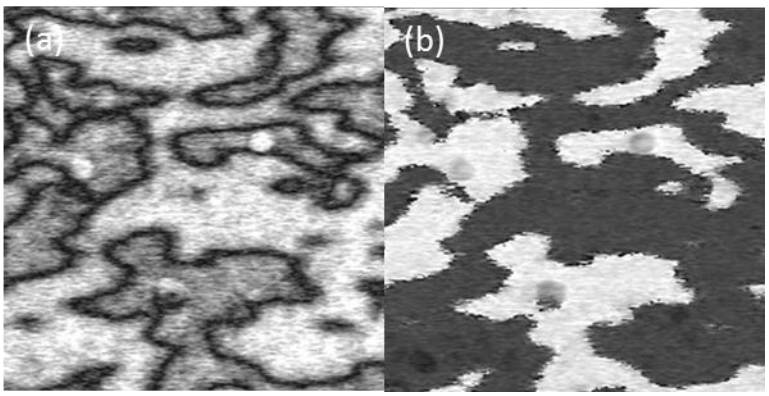

Figure 1.7 (a) the Amplitude image and (b) Phase image acquired by PFM.

The amplitude of the signal, although not employed in this work, is defined as follows. The voltage applied to the tip is shown in Equation 5, with a corresponding piezoactuation according to Equation 7. The K term, which is a function of frequency, AC bias, DC bias, and setpoint force relates to additional factors that contribute to the PFM signal: the contact area, electric field distribution, contact resonance effects on the lever, electrostatic forces, and finally the actual local electromechanical response of the sample (the converse piezoelectric effect) which reveals the local ferroelectric properties.

$$V_{tip}=V_{dc}+V_{ac}\mathbf{Cos}\ (\omega t); \quad (5)$$

$$Z_{dip}=Z_{dc}+\mathbf{K}_{\omega, V\mathbf{dc}, Vac, \mathbf{Fsp}}\ \mathbf{Cos}\ (\omega t+\emptyset); \quad (6)$$

Piezoactuation and electrostatic force in PFM is often approximated as follows:

$$\mathbf{Z} = (d_{eff} + (Lw\varepsilon_0\Delta V) / (48\mathbf{k}h_2))V_{AC}, \quad \textbf{[11]} \quad (7)$$

where h is the height of the tip, ε_0 and ΔV are the dielectric constant of the air and average voltage between the tip and the sample respectively. The second term derives from capacitive artifacts (electrostatic forces between sample and lever, not piezoactuation beneath the tip). Thus a stiff cantilever can improve the performance of the PFM signal, with the obvious caveat that it can impart damaging forces to the sample. For this reason, conducting diamond coated probes are commonly used.

Contact resonances play an important role in the performance of PFM imaging as well. Since the piezoelectric oscillation occurs at the same frequency as the applied AC voltage, it can be tuned to the frequency of highest sensitivity in an AFM, the contact resonance for the tip/lever system. More subtly, increasing the oscillation frequency for a lever effectively stiffens it, thereby reducing electrostatic (capacitive) artifacts. However, there is a limit for increasing the frequency, since the amplitudes of actuation (from artifacts, but also from the piezoresponse signal of interest) also decrease with higher frequencies. Furthermore, the AFM detector is not efficient beyond approximately 2 MHz for the AFM employed here.

As a result, when beginning a PFM measurement, a frequency sweep for the AC bias is typically achieved with the function generator. The resonant response is then easily found as the frequency with the maximum amplitude signal, ideally with a strong ratio of local electromechanical properties to noise. Such contact resonances can also be influenced by local topography, though. In particular, a larger contact area means higher tip-sample contact stiffness, which would result in a different contact resonance compared with a smaller contact area. Therefore, to minimize the chance of amplitude variations during imaging due to topographic effects instead of ferroelectric properties, the frequency for the AC bias should be chosen around the resonant peak rather than exactly at it [12].

High Speed PFM

AFM has significant applications in investigating the nucleation and growth of ferroelectric thin films. This work can provide information on the domain dynamics studies. However, in standard PFM the scan speed is not fast enough to monitor switching in-situ. High Speed PFM is a new approach which utilizes AFM probes

operated at high frequency contact resonances (>1MHz), and scanned at high speeds, providing excellent amplitude and phase contrast with a rapid image refresh rate[13]. For instance, a 1 μm x 1 μm image can be acquired in 1 second, 250 times faster than standard PFM scanning [13]. In order to achieve highest speed imaging, the HSPFM can even be scanned without feedback. High speed data acquisition is necessary as well to obtain the amplitude and phase signals with sufficient temporal (and hence spatial) resolution. As many ferroelectric materials are robust oxides, they tend to be especially amenable to such high speed property measurement.

Switching Spectroscopy PFM

Switching Spectroscopy Piezo Force Microscopy(SSPFM) approaches the switchable polarization properties of ferroelectric materials based on the hysteresis loop, providing information of positive and negative coercive voltage, saturation, switchable response and nucleation processes[14]. SSPFM also employs a standard AFM system with a Lock-in Amplifier, as well as sophisticated signal generation data acquisition electronics.

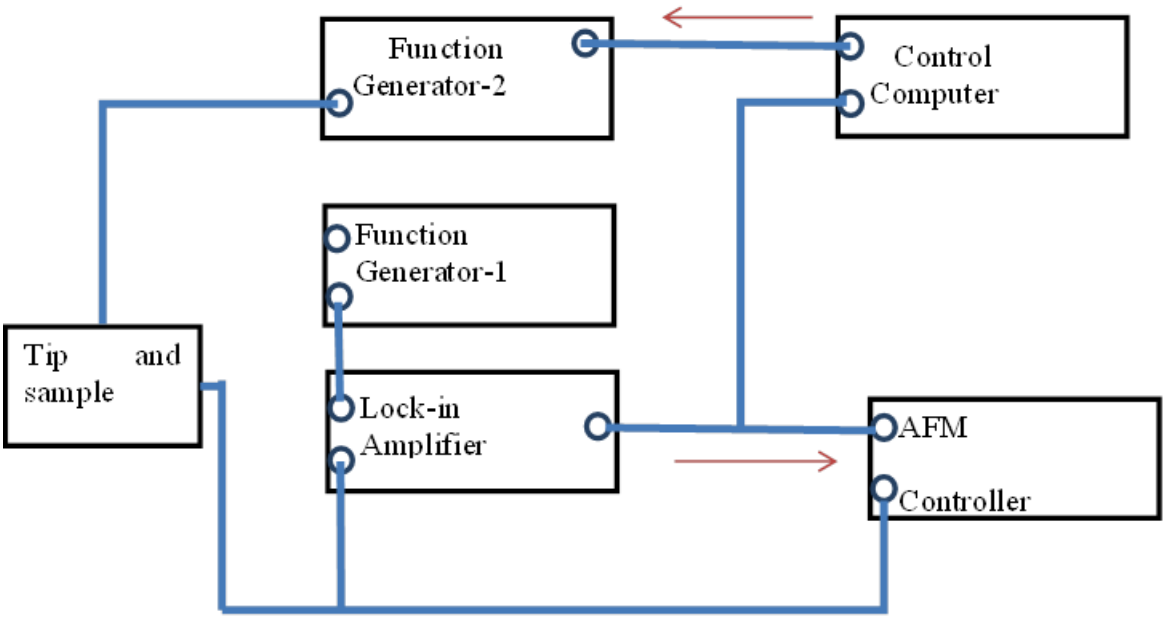

Figure 1.8 SSPFM setup.

Dual Frequency PFM

Typical amplitudes detected during PFM are on the order of picometers per volt, even for contact resonance imaging [15]. Since the topography can influence the contact resonance peak as described earlier, there can be significant crosstalk between these signals [16]. The dual AC resonance tracking mode (DART) was invented to overcome this challenge by tracking and therefore always maintaining the PFM signal at a precise frequency shift from the resonant peak.

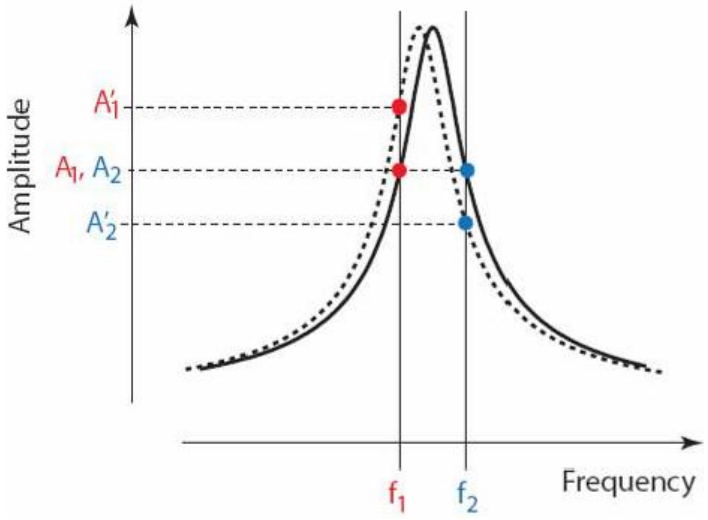

Figure 1.9 Amplitudes shift due to frequency change[17].

In the DART PFM mode, two driving frequencies f_1, f_2 are superimposed causing 2 distinct but simultaneous amplitudes of piezoresponse beneath the tip, A_1 and A_2 respectively. If the resonant frequency shifts for some reason (usually topography), the resonant frequency can be tracked because the distinct vibration amplitudes will also shift, one increasing, and the other decreasing, as shown in Figure 1.9 (A_1 - $A_2 \neq 0$). A secondary feedback loop is thus employed that shifts f_1 (and equally f_2) in order to maintain A_1 - A_2=0 at every image pixel, minimizing topographic constraints. Practically, $\Delta f = f_1 - f_2$ is often chosen such that $\Delta f \geq 2BW$, where BW is the imaging band width, around 1 kHz.

1.4 Domain Dynamics

Domain Nucleation

Significant previous research has been published investigating domain switching dynamics for ferroelectric materials, largely because the duration of the switching

determines the minimum times for reading or writing the FRAM bits and hence the ultimate device performance. One of the crucial issues is the micro and sub-micrometer dimensions of ferroelectric capacitors and their electrical parameters. The switching current and voltage also influence the results. Accordingly, Dehoff employed PFM to study FRAM cells fabricated with PZT [17]. They first negatively poled the cell, then employed a sequence of voltage pulses with increasing durations at fixed amplitudes to address the in-situ domain switching process. They found that the domain measurement can be done in capacitors as small as 1 μm^2 with 10 ns switching times.

The nucleation of domains in ferroelectrics occurs when applied external fields exceed the coercive field. The expected sites where nucleation events take place first are those locations, defects, and/or interfaces where local asymmetry, strain, charge, and/or different chemical phases lead to a much smaller nucleation energy barrier, i.e. an activation energy well.

Switching kinetics of ferroelectric domain polarization have also long been investigated, both experimentally and theoretically. The widely accepted model to address the switching nucleation and polarization was developed by Kolmogorov[18], Avrami[19] and Ishibashi[20] (KAI model). The fundamental idea of the KAI model describes that a nucleation center induces the ferroelectric domains, and this domain can grow under the electric field without restriction in an infinite ferroelectric crystals. At the initial stage, the domains grow without overlapping; but eventually the expanding domain walls eventually collide. The KAI model was developed to analytically cope with this challenge[21]:

$$\mathbf{p(t)=1-}\ e^{-(t/t_0)^n}\mathbf{,} \qquad (8)$$

where p(t) is the fraction of the switched volume in ferroelectric materials by time t, t_0 and n are parameters depending on the mobility of the domain walls, applied electric field, and dimensionality of the material and growing domain [21]. The KAI model gives a good explanation to cases of epitaxial thin films switching during a relatively short time interval, as well as switching for ferroelectric single crystals. It encounters problems when addressing more complicated cases, however.

Tagantsev et.al proposed a Nucleation-Limited-Switching(NLS) model[21]. This model is a modification and supplementation to the classic KAI model, by also addressing the switching kinetics of ferroelectric thin films over a broader time interval. The assumption is that the domain switching takes place region by region, while polarization reversal does not lead to switching of the neighboring parts. In this theory, thin films can be represented as many elementary regions, where nucleation occurs in the center of the regions and does not affect other neighboring domains. This model provides a good explanation for regions only containing a relatively few nucleation sites. The relation between the fraction of switched volume and the distribution function of the waiting time in a mathematical way is:

$$\mathbf{P(t)}=\int_{-\infty}^{\boldsymbol{Int}} \boldsymbol{g}(\boldsymbol{z})\boldsymbol{dz}; \qquad (9)$$

In Landau's theory for an ideal crystal material, the energy for reversing the polarization of the domain is very high, thousands of thermal energies (kT) in experimental results. Such tremendous values of the energy results from the energy of the depolarization field and the surface energy. While the depolarization field energy can be compensated by the free charges, the surface energy is still too large to be reduced by the thermal energies. But this conceptcontradicts the experimental observations of rapid domain nucleation

with temperature under a low electric field. Merz[22] makes a different assumption, that this nucleation is a result of thermal fluctuations, where switching proceeds when the energy to form a domain wall at the boundary between the nucleus and the remaining crystal, as well as the depolarizing field created by any bound charges at this boundary, can be overcome. Regardless, polarization reversal is a reorientation of the initial polarization under an applied external field, forming nuclei in the elementary regions. After the early stages of nucleation, this polarization reversal expands due to the continuing appearance of nuclei and the coalescence of adjacent domains.

Molotskii et.al revealed that there is a significant difference between the calculated and experimental values of the activation energies, with the experimental data much smaller than the theoretical. Therefore, they proposed another switching process to account for this discrepancy. The new hypothesis adopts that repolarization nuclei appear as bound states of electrons and polarization fluctuations[23]. This fluctuation of polarization reduces the nuclei surface energy, allowing for a reasonable value for activation energy.

Domain Growth

Four types of switching categories for single crystal, thin-film, and polycrsystalline ferroelectrics have recently been proposed [24]. They all assume that grain boundaries, defects, and/or domain wall effects can block domain growth if present. In certain cases, depending on field strength, depolarizing fields must be accounted for as well. In categories I and II, PRSPAP is inhibited mainly by grain boundaries or planes of defects such as 90º domain walls in relatively thicker epitaxial films. In categories III and IV, on the other hand, applicable to thin epitaxial films without 90 degree domain walls, switching can be influenced by adjacent switched regions, the so-called ‘Polarization

Reversal induced by the Switching Promotion effect between Adjacent Parts' model (PRSPAP)[24]. Therefore, the spatial and temporal distribution of nucleation and growth events can be an important factor in ultimate ferroelectric polarization dynamics.

Table 1: Four categories of switching models as proposed by Lou[24]:

	E_{dep} consideration	Neglecting E_{dep}
PRSPAP can be neglected	Category I: Polycrystalline thin films (or relatively thicker epitaxial films containing blocking 90º domain walls) at medium or low E_{appl} [n_{app}<1]	Category II: Polycrystalline thin films (or relatively thicker epitaxial films containing blocking 90º domain walls) at high E_{appl} or polycrystalline (ceramic) bulks [n_{app}~1]
PRSPAP has to be considered	Category III: 90º domain-wall-free single-crystalline (epitaxial) thin films at high E_{appl} or single-crystalline bulks [n_{app}≥1]	Category IV: 90º domain-wall-free single-crystalline (epitaxial) thin films at medium or low E_{appl} [n_{app}<1, ~1 or >1, it depends on the dominant factor.]

These 4 conditions influence the factor eta in Equation 10 below. Based on the non-KAI model, the duration before switching τ_{max} of the elementary regions can decrease

significantly with increasing applied field, mediated by the ratio of an activation energy (Vo) to the actual applied bias (V):

$$\tau_{max} = \tau_0 \mathbf{10}^{(V_0/V)^n} \text{ ;[21]} \qquad (10)$$

Returning to the NLS model, which explains ferroelectric switching dynamics well for thin films, it is independent of microscopic effects such as those considered by PRSPAP. More studies should be conducted to learn more about the typical size of the independent elementary regions as well as their resulting obstacles for domain wall motion. Transmission electron microscopy and PFM can be applied to investigate these problems directly in the future, but in the meantime some research groups have used macroscopic measurements and for instance KAI averaging models.

For example, So et al. employed the KAI model with epitaxial PZT thin films, which are close to the structure of single crystals, with well-ordered lattices. However, they tend to exhibit many defects, and common mismatches of the substrate and film can cause strain as well.

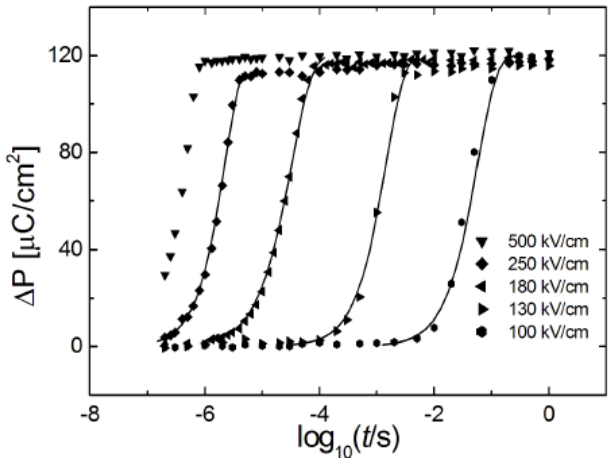

Figure 1.10 Switching behavior of the epitaxial thin film with writing pulse width[22].

Regardless of these various and sometimes inconsistent explanations about the process of polarization reversal, the fact that defects contribute to domain wall motion has been proven. In general, the NLS model accounts for this with distributions of relaxation times controlling the polarization response, while the KAI model incorporates a unique duration before switching. Each theory is free from error in its own applicable situations due to the complex process of ferroelectric thin film switching. For example, Ducharme et al. assert that the KAI model provides a correct method of the ferroelectric thin film switching process with thickness over 50nm. For ultrathin 1 nm ferroelectric films, on the other hand, the Landau-Ginzburg-Devonshire (LGD) theory of homogeneous intrinsic switching is more relevant [25].

$$\boldsymbol{\tau^{-1}=\tau_0^{-1}\exp\left(V/V_c-1\right);} \qquad (11)$$

The equation suggests that there is a threshold voltage which must be surpassed before switching can occur. In this event, polarization switching without domain formation (i.e. intrinsic) should be observed, as it is for ultrathin PZT films due to the oxygen potential change.

1.5 Crystallographic Structure

PZT

Lead Zirconate Titanate is a solid solution of $PbZrO_3$ and $PbTiO_3$. At room temperature, $PbZrO_3$ is in an orthorhombic antiferroelectric phase in which the spontaneous polarization is antiparallel in neighboring unit cells. $PbTiO_3$ at room temperature is in a tetragonal ferroelectric phase in which the spontaneous polarization is parallel in

neighboring unit cells. The $Pb(Zr,Ti)O_3$ has the ABO_3 type perovskite structure with Ti^{4+} ions and Zr^{4+} ions randomly occupying B- sites.

A tetragonal ferroelectric phase (the Ti rich region of the phase diagram) and a rhombohedral ferroelectric phase (the Zr rich region) are divided by the morphotropic phase boundary (MPB). Near the composition corresponding to the MPB, there is an abrupt change in lattice constants of PZT. Since the tetragonal and the rhombohedral phases coexist at the MPB, large piezoelectric coefficients, dielectric permittivity, and remnant polarization can be observed in this region. Anomalous properties near the MPB can be explained by a phase transition between the tetragonal and rhombohedral phases.

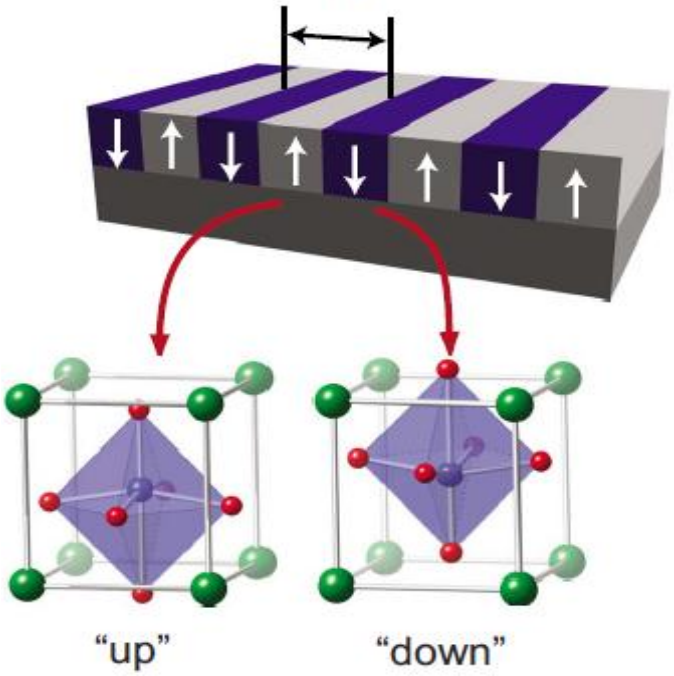

Figure 1.11 Ferroelectric materials responds according to the voltage applied[2].

$BiFeO_3$

Bismuth ferrite ('BFO') is also an oxide with perovskite structure and multiferroic material which exhibits both ferroelectric properties, ferroelastic and antiferromagnetic

properties. In general BiFeO3 has the rhombohedral crystal structure belonging to the space group R3c. For temperature below the magnetic ordering temperature, i.e. the Neel temperature, in the BFO case is around 653 K which is well above the room temperature makes the BFO material stable. Similarly the ferroelectric effect only disappears above the Curie temperature, 1100K for BFO. Ferroelectric polarization orients along the [111] direction ranging from 90 to 95$\mu C/cm^2$.

1.6 Other Relevant Techniques

Synchrotron X-ray Diffraction

X-ray diffraction has been used to study electric field induced structural deformations in ferroelectric materials for many years. In standard X-ray system, energetic electrons strike an anode and generate x-rays, but the x-ray intensity is not optimal for detecting subtle effects such as ferroelectric distortions. In the 1970s, synchrotron radiation sources solved this limitation, allowing x-ray studies that were not possible with laboratory (electron) based x-ray sources. Synchrotron radiation is based on charged electrons or positrons being accelerated around a ring by a magnetic field. X-rays are thus generated without thermal noise issues, and substantially greater brightness. In X-ray diffraction of piezoelectrics, the strain caused by the pm scale displacements of atoms under external fields (or just for oppositely oriented ferroelectric domains) leads to a change of x-ray Bragg peaks in reciprocal space and intensity. Thus piezoelectric coefficients and/or domain orientations can be measured by recording the locations in reciprocal space of Bragg reflections and their intensity.

One excellent site for such research is the Advanced Photon Source (APS) at Argonne National Laboratory. This is a third generation synchrotron x-ray source, comprising a linear accelerator, a booster synchrotron, a storage ring, and experimental halls where the x-ray experiments take place. Electrons are accelerated by a high electric field to energy of 450 MeV in the linear accelerator, after which they are transferred to a booster synchrotron where they are further accelerated to the full energy (7 GeV) of the electron storage ring. These electrons are moving at nearly the speed of light [26].

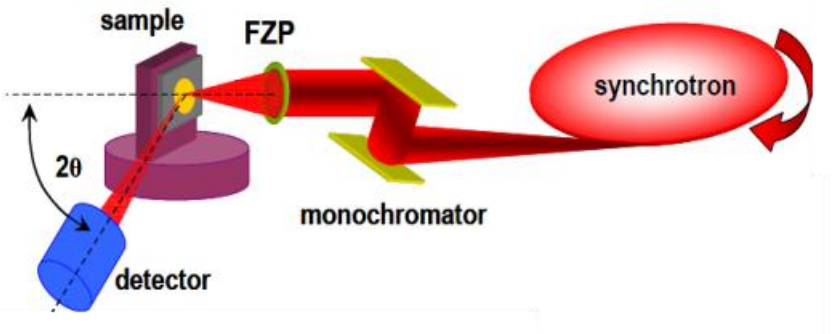

Figure 1.12 Synchrotron x-ray diffraction[27].

By monitoring Bragg reflections in reciprocal space from a focused synchrotron x-ray beam, the local displacement of atoms can be extracted with submicron resolution. Combining this approach with the ability to scan a sample thereby provides a method to map polarization switching and piezoelectricity [21].

For example, longitudinal piezoelectric distortions were measured by applying an electric field to PZT thin films in the synchrotron beam line. The converse piezoelectric effect distorts the lattice parameter, which shifts the Bragg peak angle of the PZT thin film, particularly noticeable for the (002) Bragg reflection. A shift to a higher 2θ angle occurs when the lattice contracts, while a lower angle indicates expansion. The values of the

shifts can be used to measure the longitudinal piezoelectric coefficient ($\boldsymbol{d_{33}}$) using equation 12:

$$\boldsymbol{d_{33} = \frac{\partial S_3}{\partial E_3}};\qquad (12)$$

where S_3 is the strain and E_3 is the electric field along the surface normal. Before the measurement, the researchers make the polarization vector parallel to the applied field by applying positive and negative pulses respectively on the sample. By measuring the Bragg reflection shift, the information of the piezoelectric properties and lattice change can thereby be revealed. For instance, in Figure 1.13, the (002) Bragg peak is shown decreasing below the nominal value proportional to a positive applied bias (left). When an oppositely poled domain is studied (right), a negative bias is necessary to shift the Bragg peak down.

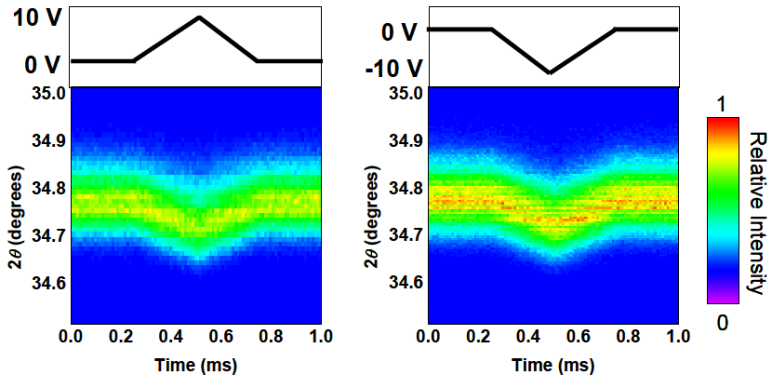

Figure 1.13 X-ray diffraction shows longitudinal piezoelectric measurement[27].

Polarization switching measurement

By applying a bipolar pulse to the sample with the antiparallel polarization vector to the external bias, the piezoelectric effect can be seen but ferroelectric switching can also be observed as long as the field exceeds the coercive field. Figure 1.14 shows ferroelectric domains first contracting (higher Bragg angles) with positive bias, then suddenly the

Bragg angle drops below the 0-Voltage case as the domain switches (t=0.4 msec). Now, higher positive voltages cause more expansion of the crystal. On decreasing the voltage, even applying negative voltages, the crystal again linearly responds with field, until the negative polarization field is reached. At this point (approximately 1.4 msec), the domain reverses again, and the lattice parameter jumps from contracted to expanded.

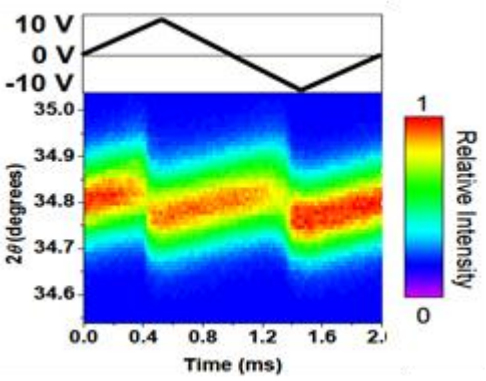

Figure 1. 14 X-ray diffraction shows polarization switching[27].

TEM

Domain dynamics have also recently been studied with TEM, providing insight into Domain orientations and even the nature of polarization switching in ferroelectric materials with locally resolved defects such as domain wall boundaries[27], domain morphology observations[28], and electric-field-induced domain switching[29]. As an example, Figure 1. 15 shows domain walls in a $BiFeO_3$ thin film.

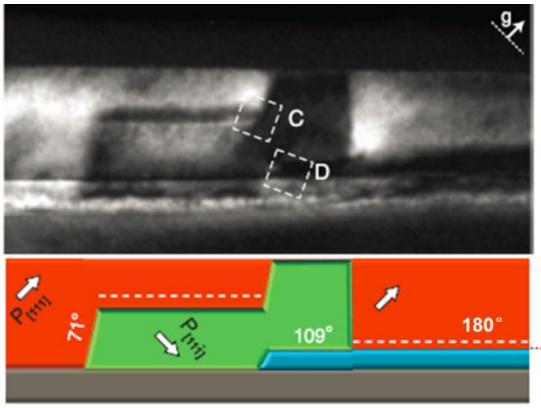

Figure 1.15 Show the 180°, 109º and 71º of domain walls in TEM[30].

For example, dynamic TEM experiments were performed using an in situ electrical biasing holder which connects to a voltage source allowing for precise control over the applied DC voltages, similar to the PFM and synchrotron approaches described above. Operating with a two-beam condition excites reflections for reciprocal lattices parallel to the projection of the polarization, providing strong diffraction contrast and hence clear imaging for distinctly oriented domains (in certain orientations). Domain walls can further be identified by visible alternating stripes of contrast. TEM thus has the potential for imaging domain wall dynamics, filling in some gaps in previous domain dynamics studies, with the obvious substantial caveats of specimen preparation that are typically serious challenges for TEM studies of functional materials.

Such TEM experiments thus far include Figure 1.16, which shows a series of TEM images captured of the real-time intermediate progression of the polarization switching for a BFO thin film. The nucleation and propagation of ferroelectric domains can thus be investigated directly, similar to high speed PFM capabilities.

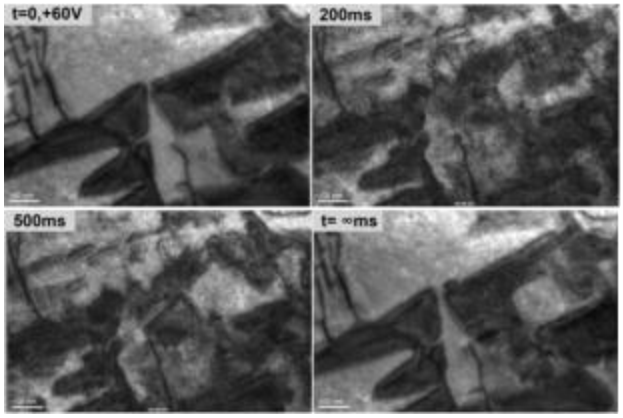

Figure 1.16 In situ biasing series in bright-field TEM, revealing the progress of the switching with applied voltage of BFO[31]

Similarly, Figure 1.17 reveals ferroelastic domain switching in a BFO thin film, revealing the occurrence of 71° and 109° ferroelectric domains as indicated. These are separately shown to shift with applied voltage.

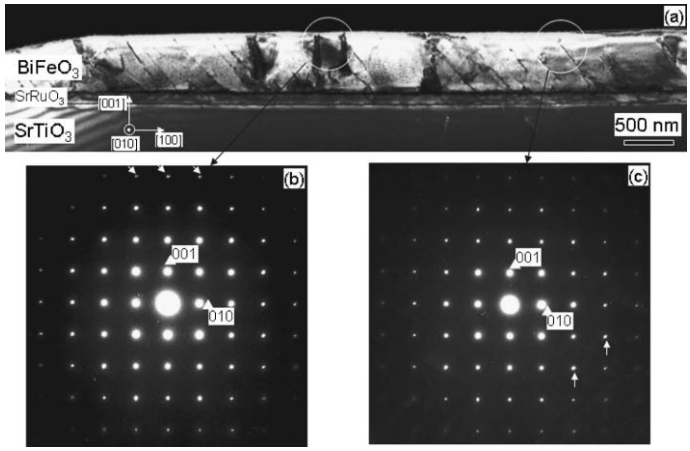

Figure 1.17 a) Typical dark field image of 600 nm BiFeO3 /100 nm SrRuO3 on (001) SrTiO3 substrate showing the 71° and 109° ferroelectric domains; b) SAED patterns from region of 109° ferroelectric domain; c) and region of 71° ferroelectric domain[32].

Cracks developing from a triple-junction pore under cyclic electric fields in PZT polycrystalline ceramics have also been studied in situ, Figure 1. 18. The initial shape of the pore was subjected to a cyclic electric field along the direction indicated by the arrow. The pore clearly expanded, extending cracks along grain boundaries.

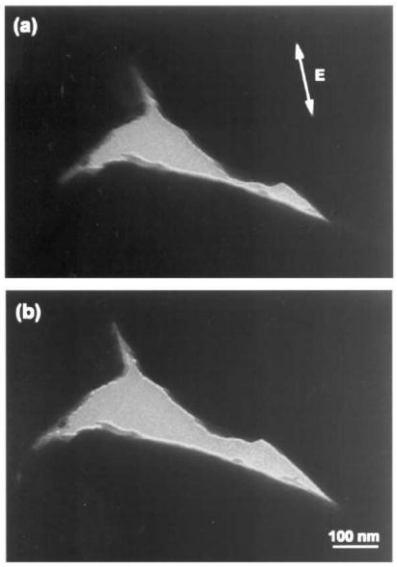

Figure 1.18 Initiation of microcrack from a pore at the triple junction of the grain boundaries of PZT thin film: (a) before application of electric field; (b) after 50 000 cycles[30].

1.7 Summary

This chapter summarizes ferroelectric domains and switching, the primary method used by other researchers to study such effects, and PFM, the main method employed in the rest of this work to investigate ferroelectric domains, domain boundaries, and their dynamics.

1.8 References

1. Frederick Seitz, T.P.D., David Turnbull, E. L. Hahn, Ferroelectrics and Antiferroelectrics, 1957, Academic Press.
2. Kholkin, A.K., Sergei; Roelofs, Andreas; and Gruverman, Alexei,, *Review of Ferroelectric Domain Imaging by Piezoresponse Force Microscopy*, 2007, Alexei Gruverman Publications. p. 46.
3. Saptarshi Das, J.A., *FETRAM. An Organic Ferroelectric Material Based Novel Random Access Memory Cell.* Nano Letters, 2011. **11(9)**.
4. Glass, M.E.L.a.A.M., *Principles and Applications of Ferroelectrics and Related Materials*. 2001, Oxford University Press.
5. Harald Ibach, H.L., *Solid-State Physics: An Introduction to Principles of Materials Science* 2003: Springer. 501.

6. Mason, W.P., *Piezoelectric Crystals and Their Application to Ultrasonics*. 1950: D. Van Nostrand Company.
7. Kaushik Bhattacharya, G.R., *Ferroelectric Perovskites For Electromechanical Actuation.* Acta Materialia, 2003. **51**.
8. Damjanovic, D., *Ferroelectric, dielectric and piezoelectric properties of ferroelectric thin films and ceramics* Reports on Progress in Physics, 1998. **61**.
9. *Atomic Force Microscopy for biological applications*.
10. Bullen, R.A.W.a.H.A., *Introduction to Scanning Probe Microscopy (SPM) Basic Theory Atomic Force Microscopy (AFM)*, 2006. p. 8.
11. Partner, N.S., *Piezoelectric Force Microscopy (PFM)*. p. 6.
12. STUTT, C.A., *Low-Frequency Spectrum of Lock-in Amplifiers*, 1949, Massachusetts Institute of Technology. p. 22.
13. Partner, N.S.
14. Bryan D. Huey, R.N.P., Sungjun Lee, Nicholas A. Polomoff, *High Speed SPM Applied for Direct Nanoscale Mapping of the Influence of Defects on Ferroelectric Switching Dynamics.* Journal of the American Ceramic Society, 2012. **95**(4).
15. Stephen Jesse, H.N.L., and Sergei V. Kalinina, *Quantitative mapping of switching behavior in piezoresponse force microscopy.* American Institute of Physics, 2006. **77**.
16. Research, A., *Piezo Force Microscopy using Dual AC Resonance-Tracking*, 2010. p. 17.
17. Brian J. Rodriguez, C.C., Sergei V. Kalinin, and Roger Proksch, *Dual-Frequency Resonance-Tracking Atomic Force Microscopy*, Materials Science and Technology Division and The Center for Nanophase Materials Sciences, Oak Ridge National Laboratory. p. 15.
18. C. Dehoff, B.J.R., A. I. Kingon, R. J. Nemanich, A. Gruverman, *Atomic force microscopy-based experimental setup for studying domain switching dynamics in ferroelectric capacitors.* American Institute of Physics, 2005. **76**.
19. A.N. Kolmogorov, I.A.N., Ser. Math, 1937. **3**.
20. M. Avrami, J. Chem. Phys, 1940: p. 8.
21. H. Orihara, S.H., and Y. Ishibashi,, J. Phys. Soc. Jpn, 1994. **63**.
22. Alexander K. Tagantsev, I.S., and Nava Setter, *Non-Kolmogorov-Avrami switching kinetics in ferroelectric thin films.* PHYSICAL REVIEW, 2002.
23. Merz, W.J., *Domain Formation and Domain Wall Motions in Ferroelectric BaTiO3 Single Crystals.* Phys. Rev, 1954. **95**(3).
24. M. Molotskii, R.K., and G. Rosenman, *Fluctuon effects in ferroelectric polarization switching.* JOURNAL OF APPLIED PHYSICS, 2000. **88**.
25. Lou, X.J., *Four switching categories for thin-film and bulk ferroelectrics*, Department of Materials Science and Engineering, National University of Singapore, 117574, Singapore. p. 13.
26. S. Ducharme, V.F., R. Gaynutdinov, M. Minnekaev, A. Tolstikhina and A. Zenkevich, *Homogeneous switching in ultrathin ferroelectric BaTiO3 films.* 2012.
27. Do, D.-H., *Investigation of ferroelectricity and piezoelectricity in ferroelectrics thin film capacitors using Synchrotron X-ray Diffraction*, 2006, University Of Wisconsin-Madison.
28. Gleiter, T.M.a.H., *Investigation of the structure of ferroelectric domain boundaries by transmission electron microscopy.* JOURNAL OF APPLIED PHYSICS, 1976. **47**.
29. Cheuk Wai Tai, S.H.C., Helen L. W. Chan, *Ferroelectric Domain Morphology Evolution and Octahedral Tilting in Lead-Free (Bi1/2Na1/2)TiO3–(Bi1/2K1/2)TiO3–(Bi1/2Li1/2)TiO3–BaTiO3 Ceramics at Different Temperatures.* Journal of the American Ceramic Society, 2008. **91**(10).

30. Xiaoli Tan, Z.X., Jian Ku Shang, *In situ transmission electron microscopy observations of electric-field-induced domain switching and microcracking in ferroelectric ceramics.* Elsevier Science, 2001.
31. C.R. Winklera, A.R.D., J. Karthikb, L.W. Martinb, M.L. Taheria, *Direct observation of ferroelectric domain switching in varying electric field regimes using in situ TEM.* Micron, 2012. **43**.
32. Y. B. Chen, M.B.K., X. Q. Pan, R. R. Das, D. M. Kim, *Ferroelectric domain structures of epitaxial (001) BiFeO3 thin films.* Applied Physics Letters, 2007. **90**.

Chapter 2. Materials and methods

2.1 AFM

The AFM utilized to accomplish the experiments is an Asylum Research MFP-3D High-Resolution AFM, with Igor Pro software version 6.22A. All experiments were performed at room temperature and in air. The piezoactuator scanners on the MFP-3D system have a maximum range in the X and Y directions of 80 μm and a 15 μm extension range in the Z direction.

Figure 2.1 AFM in the Nano-measurement lab.

As with nearly all AFM systems, the AFM tip is integrated with a cantilever that deflects due to various interactions with a specimen, and which is detected optically (Figure 2.2). Technically, a super bright infrared LED is reflected from the lever onto a quadrant segmented photodiode. The position of the reflected laser spot is then simply recorded, indicating the normal or lateral (torsional) deflection of the lever.

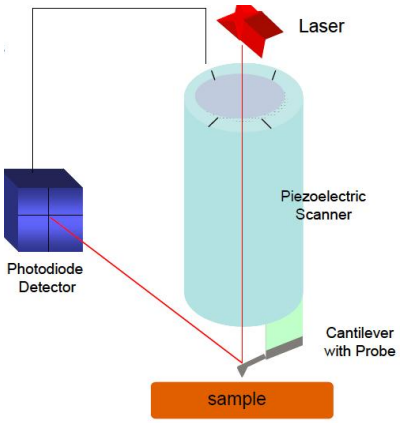

Figure 2.2 AFM imaging set up[1].

2.2 Lock-in Amplifier

The Lock-in Amplifier (LIA) is a Stanford Research System Model SR844 RF Lock-in Amplifier. Small output PFM signals, along with the substantially larger background noise, are filtered by synchronizing (locking in) to the function generator AC frequency. The LIA recovers the PFM electromechanical signals and amplifies them over several orders of magnitude as necessary.

Figure 2.3 Stanford Lock-in Amplifier system.

In its simplest form, a LIA operates by comparing an input signal with a reference sin or square wave that is supplied either internally or externally (typically by a function generator as employed here). In order to amplify the information contained in the input signal ($V_{in} = Asin(\omega t + \varphi)$) at the frequency of the reference signal ($V_{ref} = Bsin(\omega t)$),

the two signals are actually multiplied together, known as demodulation. This results in Equation 13:

$$\boldsymbol{V_{out} = \frac{1}{2}ABsin(\varphi) + \frac{1}{2}ABsin(2\omega t + \varphi);} \qquad (13)$$

where *A* is the input signal Amplitude and *B* is the reference signal Amplitude, ω is the frequency of the reference signal and the frequency of interest in the noisy input signal, and φ is any phase shift between the two signals. This output has an AC component and a DC component, which can be filtered to eliminate the time dependent 2ω component. Finally the unknown amplitude A can be determined after integrating this output signal over a period of time defined as the Time Constant, τ, which is essentially a running average of the lock-in output [30].

The time constant in a LIA is a user-selectable parameter that defines, to first-order, how quickly the unit can respond to (detect) an impulse. Technically, the time constant is the time required to complete 63.2% of the rise or decay impulse. Better results are always achieved by integrating (averaging) as long as possible. However, practical measurements such as with an AFM cannot extend indefinitely. In fact, the scanning tips spend only a limited amount of time per pixel, summarized in the third column of Table 2 depending on the AFM scanning line rate (1st column). For optimal spatial resolution, the time constant in the lock-in should therefore always be approximately this value: any less and the signal is not being averaged sufficiently long, causing images with speckle noise; any more and the results from adjacent pixels are averaged together, leading to a 'smeared' image. Assuming an optimal time constant is selected, the tip and lever can then oscillate a maximum number of times per pixel as indicated in the table body, which naturally depends on the excitation frequency (last 6 columns, usually in the 100 kHz to 2

MHz range). As a rule of thumb, at least 4 cycles per pixel are necessary for reliable results, though standard AFM imaging typically relies on hundreds to thousands of cycles per pixel.

Table 2: Summary of the number of AFM tip oscillations per pixel at various AFM scanning rates (rows) for specific oscillation frequencies (columns).

			frequency(kHz)					
rates(Hz)	res(pixels)	usec/pixel	2000	1000	333.3	200	142.9	100
0.1	256	19531.25	39063	19531	6510.4	3906.3	2790.179	1953.1
0.2	256	9765.625	19531	9765.6	3255.2	1953.1	1395.089	976.56
5	256	390.625	781.25	390.63	130.21	78.125	55.80357	39.063
1	256	1953.125	3906.3	1953.1	651.04	390.63	279.0179	195.31
2	256	976.5625	1953.1	976.56	325.52	195.31	139.5089	97.656
5	256	390.625	781.25	390.63	130.21	78.125	55.80357	39.063
8	256	244.140625	488.28	244.14	81.38	48.828	34.87723	24.414
10	256	195.3125	390.63	195.31	65.104	39.063	27.90179	19.531
20	256	97.65625	195.31	97.656	32.552	19.531	13.95089	9.7656
40	256	48.828125	97.656	48.828	16.276	9.7656	6.975446	4.8828
80	256	24.4140625	48.828	24.414	8.138	4.8828	3.487723	2.4414
100	256	19.53125	39.063	19.531	6.5104	3.9063	2.790179	1.9531

A phase shift between the reference and detected signals is also likely, which for PFM is critical to determining domain orientations. Figure 2.4 compares typical reference, detected, and multiplied signals, where the signal slightly leads the reference. Note that the amplitudes here are relative—they need not be identical (and very seldom are).

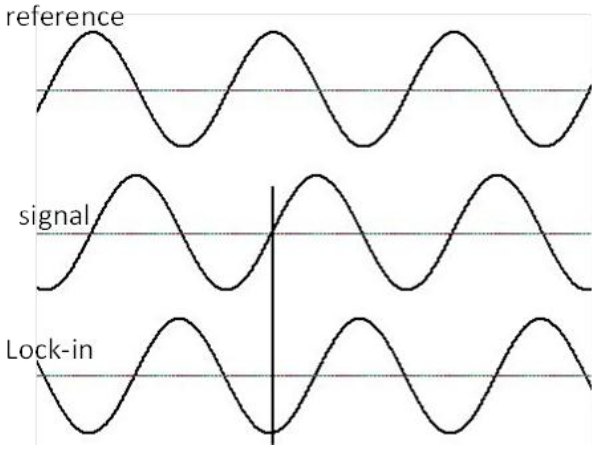

Figure 2.4 Refrence wave and signal wave.

For the LIA employed here, the amplitude and phase shift are actually extracted using a two phase detection system, which essentially performs the same procedure twice, once as described, and again but with a reference signal that is phase shifted by 90 degrees. The resulting in-phase ($X = V_{sig}\cos\theta$) and quadrature components ($Y = V_{sig}\sin\theta$) are then analyzed to determine the signal amplitude and phase as follows in Equations 14 and 15.

$$\mathbf{R} = \sqrt{\boldsymbol{X^2 + Y^2}} = \boldsymbol{V_{sig}} \qquad (14)$$

$$\boldsymbol{\theta} = \mathbf{arctan}(\mathbf{Y/X}) \qquad (15)$$

Figure 2.5 LIA panels for Amplitude (left, AFM Input channel 0) and Phase (right, AFM input channel 1) signals.

Next, the detected amplitude (R) and phase (theta) are amplified by a user-selectable sensitivity setting, which is based on a lower (usually 0 V_{rms}) and upper (typically 10-30 mV_{rms}) range of detected amplitudes to detect. Ideally, the upper range is approximately a factor of 3 higher than the strongest signal detected in any given measurement, to avoid maxing out the detector. In any case, the lower to upper range is used to scale the actually detected signals between -10 and +10 Volts of output from the lock-in amplifier, which can then be read by the AFM through input ports 'In0' (typically for amplitude) and 'In1' (typically for phase). These signals update every time constant, and are sampled every pixel by the AFM electronics. To convert the values recorded by the AFM from the lock

in, Equations 16 and 17 are finally necessary. Of course LIA detected amplitudes and phases can also simply be recorded directly, without needing to be concerned about such scaling factors. However, by reading the constantly updating signals in real time with the AFM, amplitude and phase images can be acquired simultaneously with topography, easing operation and analysis of PFM experiments.

$$\boldsymbol{Amplitude_{V,rms}} = \frac{\boldsymbol{In_0 * Sensitivity_{V,rms}}}{\boldsymbol{10}} \qquad (16)$$

$$\boldsymbol{Phase_{degrees}} = \frac{\boldsymbol{In_0 * 180}}{\boldsymbol{10}} \qquad (17)$$

2.3 Function Generator

The function generator used here is an Agilent 33250A 80 MHz Function/Arbitrary Waveform Generator. This device has two primary connections, including the bias source used to pole and or piezoactuate the tip/sample, and a synchronization square wave at exactly the same AC frequency which is used by the LIA as described above.

Figure 2.6 Function generator.

AC sinusoidal voltages cause the surface to vibrate by the converse piezoelectric effect as described in Chapter 1, allowing domain orientations to be mapped. A DC only voltage may separately be applied, usually to pre-pole a domain pattern as long as the bias exceeds the coercive field. Superimposed DC and AC voltages are also often applied in

this work, to simultaneously achieve ferroelectric domain poling and detection. The maximum voltage that can be applied from the function generator is 10 V, typically at frequencies of approximately 500-2000 kHz.

2.4 AFM Probes

The primary cantilever used in the experiments is a conductive diamond coated tip, type CDT-NCHR, acquired from Nanoworld, Figure 2.7. The nominal cantilever length is 120-130 μm, with a resonant frequency of 280-510 kHz and spring constant between 42-142 N/m. A custom PFM cantilever-holder is used which incorporates a wire connecting the output voltage from a function generator directly to the tip. Wires are also silver painted to the back electrode on the sample for connection to the ground return to the function generator.

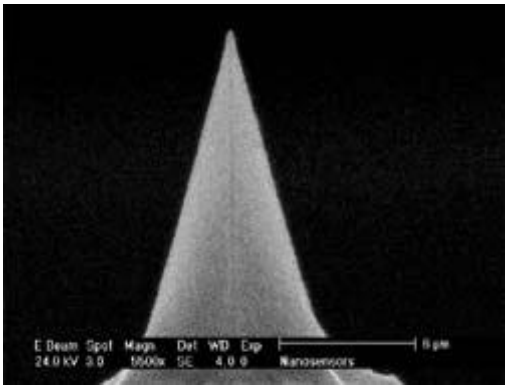

Figure 2.7 Probe shape in SEM image[31].

The conductive diamond coated high resonance frequency tip (CDT-NCHR) possesses high operation stability, and is mechanically robust. The strength and hardness of this AFM probe is especially beneficial for high speed PFM scanning, as tip damage is minimized. The probes are conductive as the diamond coating is actually highly doped with Boron, providing a total resistance measured in contact to a platinum surface of less

than 10 kOhm. The typical pyramid tip radius of curvature is between 100 nm to 200 nm, which for normal setpoint contact forces leads to a contact area on the order of 10 nm. The detector side of the cantilever is coated with 30 nm of aluminum to enhance the reflectivity of the optical lever detection beam.

2.5 Resser

Resser is a frequency sweeping program designed by David Schuman, a previous lab member. This is a convenient tool for detecting contact resonances during PFM. This contact resonance is mainly related to the stiffness of the sample surface, the lever stiffness, the setpoint force, and the contact area. Since this can vary from experiment to experiment, the program was developed to automatically sweep a range of frequencies with the function generator, record the results from the lock-in amplifier, and plot the output. This helps to identify amplitude peaks and 180 degree phase shifts which occur at resonances, thus easing the acquisition of quality images.

2.6 Resonance Frequency

An example of a contact resonance during a PFM measurement is shown in Figure 2.8, which displays the vertical piezoelectric signal as a function of drive frequency. The resonant frequency itself, here approximately 600 kHz, is usually roughly 7 times the free resonance of the lever. For the probes implemented in these experiments, the frequency for the out-of-plane (OP) signal is between 1300 kHz ~ 1500 kHz, while the in-plane (IP) signal is at ~ 1700 kHz.

Figure 2.8 An example of a Normal PFM peak.

2.7 PFM Signal

PFM Amplitude and Phase contrast

In a PFM amplitude image, contrast represents the magnitude of the local piezoactuation. Domain walls can be seen as the low-contrast features between adjacent domains, essentially where the tip is half way above a domain that is oscillating in phase, and half way above a domain oscillating out of phase. Phase contrast, on the other hand, is basically binary, with a range of 180 degrees for domains oriented parallel to the detected direction (normal or lateral), or antiparallel.

Vertical and Lateral PFM

The AFM cantilever is most sensitive to displacements or vibrations normal to the sample surface (and cantilever plane). 'Vertical' PFM detects this signal, along the z axis. The cantilever can also torque along one axis (x axis), which can be separately or even simultaneously monitored as the 'Lateral' or 'In-Plane' PFM response. Technically the lever can also buckle along the other (transverse) in-plane direction (the y axis), but this mode is exceptionally stiff and thus is seldom monitored by the AFM community due to extremely low signal: noise ratios.

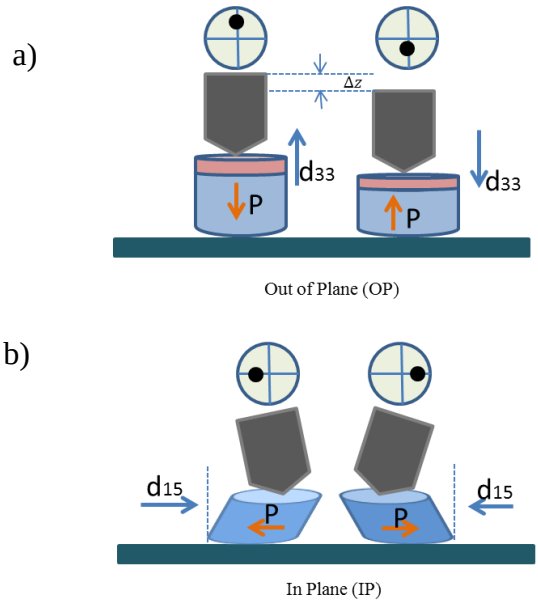

Figure 2.9 a) shows the demonstration of the out of plane (vertical) signal; b) shows the in plane (lateral) signal.

Figure 2.10 displays an example of phase contrast for such out of plane (left) and in plane (right) PFM images. Some of the regions have the same high or low contrast, while others are distinct for one image versus the other. This is because the domains in this specimen can be oriented along several different directions within the surface plane.

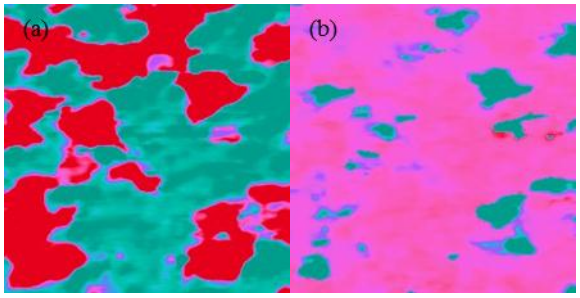

Figure 2.10 (a) Vertical and (b) Lateral Phase data.

To truly identify the orientation of such domains, the same region would have to be imaged again after sample rotation by 90°. A vector analysis of the signals can then be employed to determine the exact piezoactuation vector in 3 dimensions, presuming the lateral and normal amplitudes are properly calibrated. Practically, however, this

calibration is a challenge. Fortunately, though, for certain specimens such as epitaxial films or single crystals, the full vector analysis is not actually required. In these samples, only certain domain orientations are possible related to the ferroelectric polarization axes in the unit cell. As a result, domain orientations can be extracted without a full amplitude analysis, instead relying simply on the phase contrast which does not require difficult calibrations whatsoever.

2.8 PZT Sample

The samples used in this experiment are a PZT thin film from the Ramesh lab at the University of California, Berkeley. Epitaxial $PbZr_{0.2}Ti_{0.8}O_3$ (PZT) tetragonal films are grown on $SrTiO_3$ with intermediate $SrRuO_3$ conducting electrodes. The PZT is approximately 50 nm thick, so the film exhibits domains oriented normal to the surface only (no in-plane domains or film relaxation has been detected).

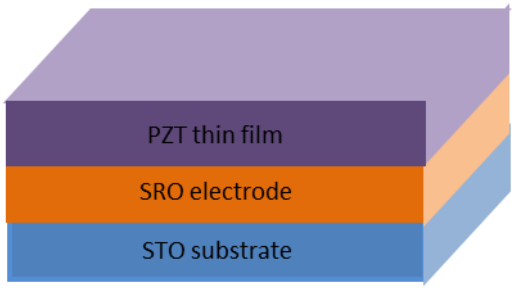

Figure 2.11 PZT thin film.

2.9 BFO Sample

The BFO samples used in the experiment are $BiFeO_3$ thin film on top of the $SrTiO_3$ with $SiRuO_3$ electrode. In the 8 domain variant sample, it's a 50 nm epitaxial BiFeO3 thin film, grown on the (001) single crystal SrTiO3 substrate[32].

In the 4, 2 and 1 domain variant samples, Films were prepared using adsorption controlled reactive molecular-beam epitaxy (MBE) on (001)-oriented non-vicinal, and vicinal 4º miscut along [100], and vicinal 4º miscut along [110] SrTiO3 substrates, with a 30 nm thickness[33].

2.10 Summary

This chapter discusses the equipment, software and probe that has been utilized in the experiment as well as the specimen. Furthermore, the PFM signal has been illustrated here and how to acquire ferroelectric information from them is also described briefly.

2.11 References

1. Sergei V Kalinin, A.N.M., Long Qing Chen and Brian J Rodriguez, *Local polarization dynamics in ferroelectric materials.* Reports on Progress in Physics, 2010. **73**.
2. Nanosensors, Diamond Coated PointProbe® Plus Silicon-SPM-Probes, 2002, Nanosensors. p. 4.
3. Joseph Desmarais, J.F.I., Tassilo Heeg, Jürgen Schubert, Darrell G. Schlom, *Mapping and statistics of ferroelectric domain boundary angles and types.* Applied Physics Letters, 2011. **99**(16).
4. Patrick E. Hopkins, C.A., Linghan Ye, Bryan D. Huey, Stephen R. Lee, Effects of coherent ferroelastic domain walls on the thermal conductivity and Kapitza conductance in bismuth ferrite. Applied Physics Letters, 2013. **102**(12).

Chapter3. $BiFeO_3$ Domain and Domain Wall Analysis

For $BiFeO_3$, the <111> polarization directions allow for up to 8 polarization orientation variants. This reduces to 3 possible polarization angles at interfaces between domains: 180°, 109°, and 71°. 4 possible domain boundary types or configurations are also possible, where ‘head-to-head’ or ‘tail-to-tail’ interfaces experience opposing electric fields and are charged, while ‘head-to-tail’ or ‘tail-to-head’ domains are charge-neutral. It is important to understand and ultimately control these interface types as they may influence electronic and thermal transport, ferroelectric performance, and reliability. Two experiments have been performed along these lines, one for a single sample exhibiting all 8 possible polarizations (known as a ‘4-domain variant’ condition), and another using 3 samples representing 4, 2, and 1 domain variants.

3.1 $BiFeO_3$ 8-domain Variant

This chapter presents methods for the measurement and analysis of such domain and domain boundary polarizations. As described previously, this is achieved using PFM to detect the out of plane (OP) and in plane (IP) piezoresponse. To fully characterize all possible domain orientations in epitaxial BFO, the sample must then be rotated by 90 degrees and re-measured at the same location. An example of the two distinct in plane PFM images, and their simultaneously acquired out of plane piezoresponses (which should be identical), follows as Figure 3.1. This procedure is explained thoroughly below.

The data is acquired for an epitaxial, 50 nm thick, $BiFeO_3$ film, grown on a single-crystal $SrTiO_3$ substrate by the Ramesh group at UC Berkeley as detailed in Chapter 2.

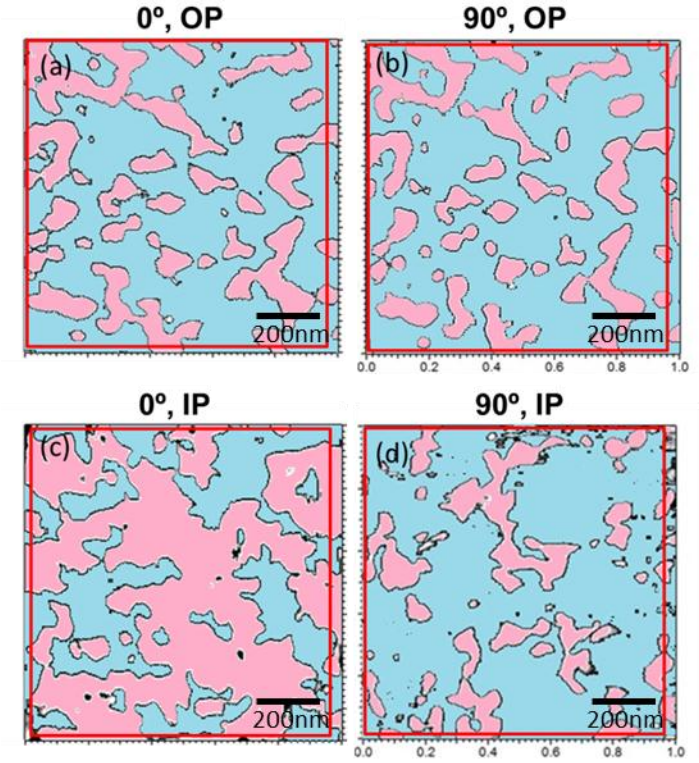

Figure 3.1 PFM images of an 8-variant BiFeO3 specimen (a) out-of-plane image at 0°, (b) in-plane image at 90°, (c) out-of-plane image at 90°, and (d) in-plane image at 90°.

Practically this experiment is performed by acquiring 1 µm x 1 µm OP and IP PFM images with the sample oriented at 0 degrees, then a larger area of ~20 µm is imaged to provide an overview of the scanned vicinity. An optical image of the AFM tip and imaged region is also acquired with a much wider field of view for the same purpose. Figure 3.2 exemplifies this result, along with sketches indicating the possible domain orientations identified by the detected OP and IP contrast. For example, regions with white OP contrast possess domains oriented normal to the surface as sketched at top right, with vectors of <h,h,1> where h can be ±1. There are 4 possible such domains. The dark OP contrast also identifies 4 possible domain orientations, but into the plane instead

of out of it. The IP PFM image similarly identifies 4 possible orientations, either <1,k,k> or <-1,k,k> for white or dark contrast, respectively. Combining this data, the possible orientations for every single pixel in the image can be reduced to pairs of two domains. For instance, white OP contrast and white IP contrast for this 0° rotated specimen represents <1,k,1> domains that point up out of the plane, and forwards in plane, in other words following the yellow or orange vectors in the upper right sketch ([1,1,1] or [1,-1,1], respectively).

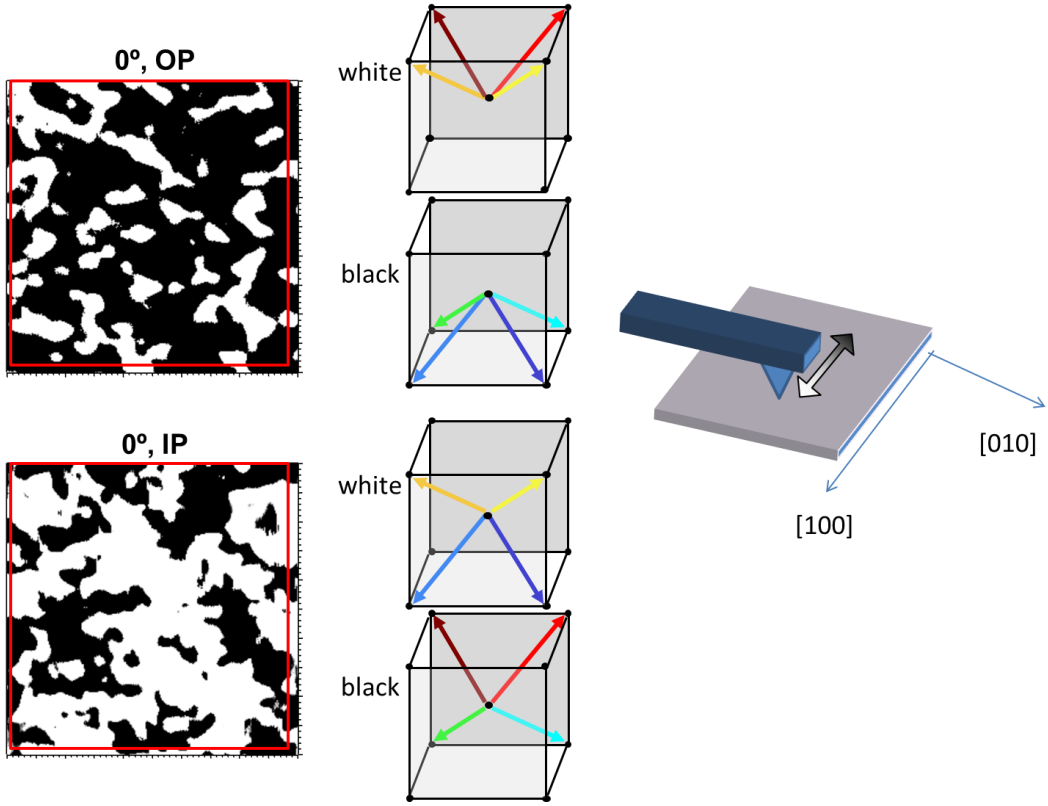

Figure 3.2 Black and white PFM contrast for 0º oriented specimen corresponds to certain sets of 4 possible polarization orientations.

Next, the specimen is physically rotated by 90^0, and all optical and AFM images from the 0° oriented sample are similarly rotated by 90^0 in the computer to ease visual comparisons. A large area PFM image is then acquired to get close to the same specimen

location as was previously imaged at 0°, and the surface is progressively rescanned with increasingly higher magnifications until the previously imaged 1μm area is found. Finally, these high resolution OP and IP PFM images are once again acquired, but from this new perspective rotated by 90°. The OP PFM images are the same since for 0° and 90º specimen rotations the domains are still pointing in or out of the plane of the sample. However, the lateral data may change for the two specimen rotations. In the specific example described earlier for white OP contrast and white 0° IP contrast, the new 90° IP contrast completes the identification of the specific polarization direction, with white regions oriented [1,1,1] and black regions oriented [1,-1,1] showing in Figure 3.3.

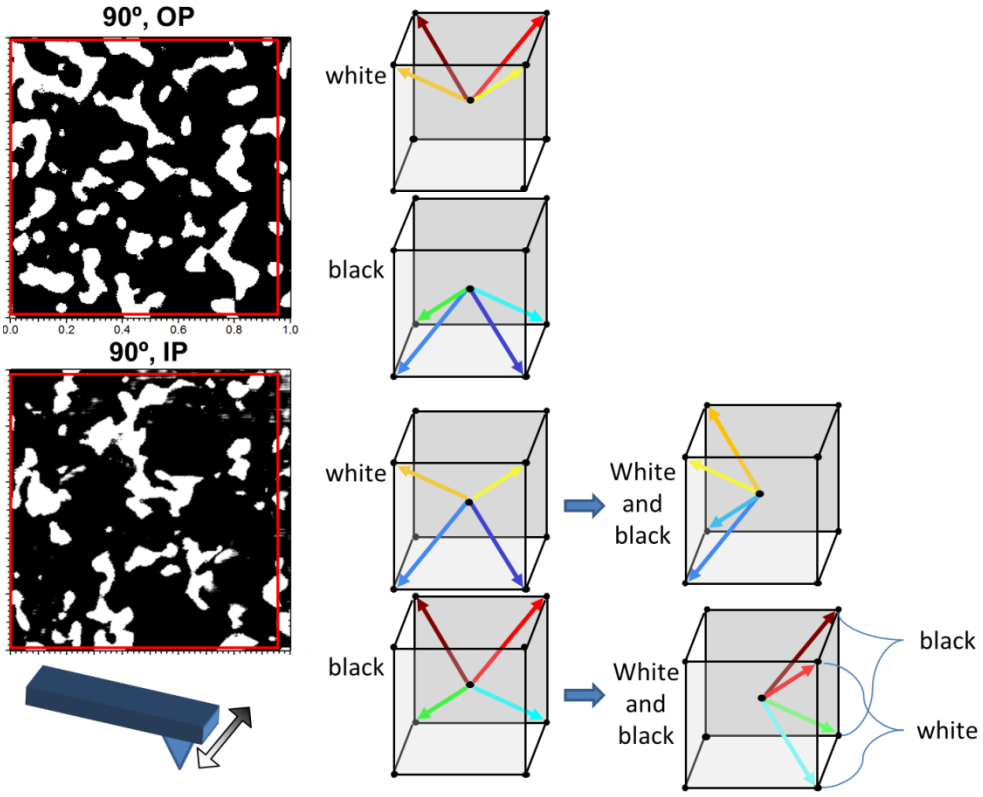

Figure 3.3 Black and white PFM contrast for 90º oriented scanning completes identification of polarization orientations.

Of course this procedure can be followed for all other domain orientations as well, as has been done by several authors for a handful of domains. To statistically analyze domain and domain wall distributions, however, this process has been automated using custom Matlab code. The software considers the OP, IP(0^0), and IP(90^0) contrast for every single pixel, comparing these signals against Table 3 below to determine the specific domain orientation for each location. This table assumes the PFM IP images are acquired along [±1,0,0] and [0, ±1,0] directions, while an equivalent table is used if IP piezoresponse is acquired along [±1, ±1,0] vectors.

Table 3: Lookup table for determining domain orientations for (001) oriented ferroelectrics with <1,1,1> polarization directions such as BFO, assuming IP piezoresponse acquired along [±1,0,0] and [0, ±1,0] directions.

orientation	Vertical (0°,90°)	Lateral 0°	Lateral 90°
$[1\bar{1}1]$	White	White	Black
$[\bar{1}\bar{1}1]$	White	Black	Black
$[\bar{1}11]$	White	Black	White
[111]	White	White	White
$[\bar{1}\bar{1}\bar{1}]$	Black	Black	Black
$[1\bar{1}\bar{1}]$	Black	White	Black
$[11\bar{1}]$	Black	White	White
$[\bar{1}1\bar{1}]$	Black	Black	White

Applying this table to all ~65,000 pixels in the overlapping data from Figure 3.1(within the overlain red squares), a map of the ferroelectric domain orientations in all 8 directions has been determined. Careful inspection of Figure 3.4 reveals a nearly equal proportion of each domain variant. Interestingly, there seems to be clear variations in the typical domain size for certain variants.

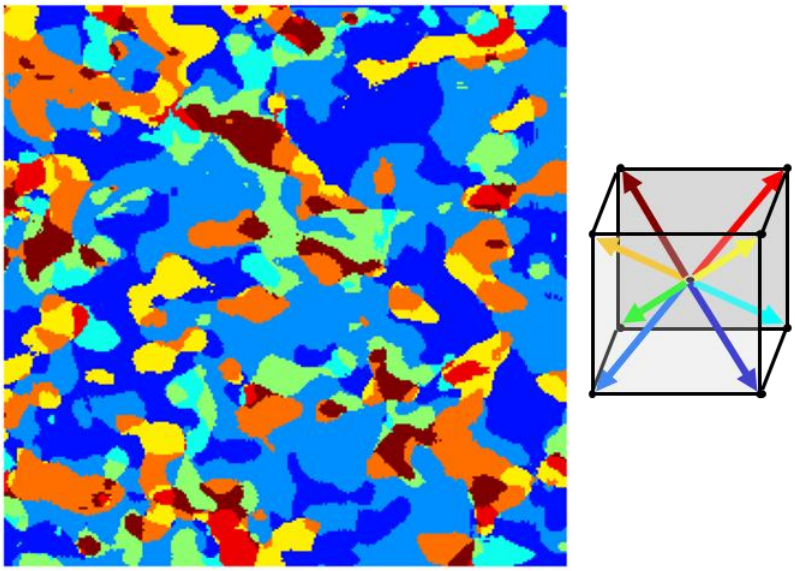

Figure 3.4 Domain orientation map color coded with all 8 possible polarization directions.

With a map of all possible domain orientations, it is also possible to determine the locations of all domain boundaries. Moreover, another lookup table can be implemented to determine the specific polarization angles at each interface between adjacent domains, Table 4. For any given domain, its neighbors can be 180° out of plane (full ferroelectric switching), or 71° or 109°, either of which can be ferroelastic, ferroelectric, or a combination of the two.

Table 4 identifies which domain boundaries exhibit which angles based on conventional orientation notations, which are related to the 4 possible polarization directions as noted where '+' indicates those domains poled away from the surface [hk1] and '-' represents domains into the surface [hk-1].

Table 4. Polarization angle at domain walls, determined by matching the domain orientation with the adjacent domain's orientation.

polarization direction	orientation convention	71 degree domain boundaries			109 degree domain boundaries			180 degrees
$[\bar{1}\bar{1}1]$	p_3^+	p_1^-	p_4^+	p_2^+	p_2^-	p_4^-	p_1^+	p_3^-
$[\bar{1}11]$	p_2^+	p_4^-	p_1^+	p_3^+	p_3^-	p_1^-	p_4^+	p_2^-
$[1\bar{1}1]$	p_4^+	p_2^-	p_1^+	p_3^+	p_3^-	p_1^-	p_2^+	p_4^-
$[111]$	p_1^+	p_3^-	p_4^+	p_2^+	p_2^-	p_4^-	p_3^+	p_1^-
$[\bar{1}\bar{1}\bar{1}]$	p_1^-	p_2^-	p_4^-	p_3^+	p_3^-	p_4^+	p_2^+	p_1^+
$[\bar{1}1\bar{1}]$	p_4^-	p_3^-	p_1^-	p_2^+	p_2^-	p_1^+	p_3^+	p_4^+
$[1\bar{1}\bar{1}]$	p_2^-	p_3^-	p_1^-	p_4^+	p_4^-	p_1^+	p_3^+	p_2^+
$[11\bar{1}]$	p_3^-	p_2^-	p_4^-	p_1^+	p_1^-	p_4^+	p_2^+	p_3^+

Figure 3.5 presents a map of the domain walls, with their color indicating the rotation angle between adjacent domains. For this BFO specimen, nearly all domain wall angles are 71°. This is not surprising as such domain wall angles are expected to have the lowest energy of all possible transitions[32].

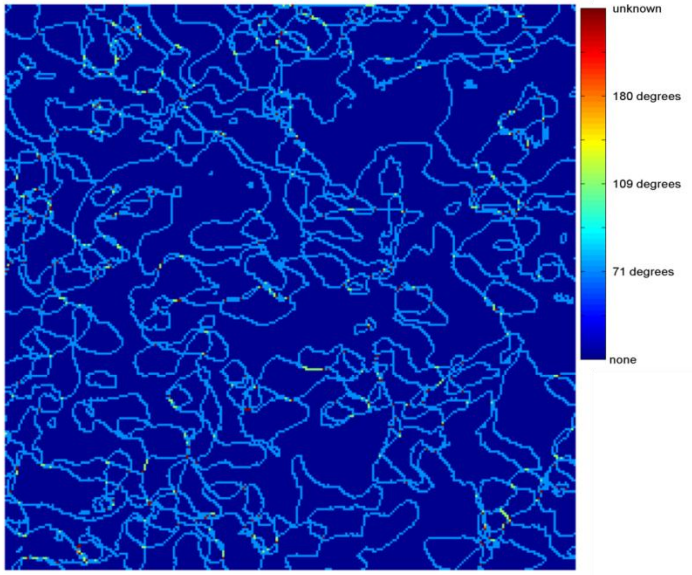

Figure 3.5 Map of domain boundary positions and angle.

Knowing the domain orientations on either side of every domain boundary also allows one to identify the domain wall type and charging, where Head-Head and Tail-Tail boundaries are charged, but Head-Tail and Tail-Head interfaces are neutral. Carefully

considering the domain maps, the domain wall type is found to depend as much on the orientation of the domain wall as it toes on the adjacent domain orientations. Vertical (y oriented) boundaries can (but do not always) exhibit a different configuration than horizontal (x oriented) boundaries. The necessary lookup table, Table 5, is therefore more complicated than Table3 and Table 4, but again mat lab code automates this procedure so that it can efficiently be employed for statistical analyses of entire images or sets of images.

Table 5. Domain boundary type (head to head, head to tail, etc) for domain wall direction

polarization direction	orientation convention	vertical boundary: HH (shaded) or TT				vertical boundary: HT (shaded) or TH			horizontal boundary: HH (shaded) or TT				horizontal boundary: HT (shaded) or TH		
$[\bar{1}\bar{1}1]$	p_3^+	p_4^-	p_1^+	p_2^+	p_3^-	p_2^-	p_1^-	p_4^+	p_2^-	p_1^+	p_4^+	p_3^-	p_4^-	p_1^-	p_2^+
$[\bar{1}11]$	p_2^+	p_1^-	p_4^+	p_3^+	p_2^-	p_3^-	p_4^-	p_1^+	p_3^-	p_1^+	p_4^+	p_2^-	p_4^-	p_1^-	p_3^+
$[1\bar{1}1]$	p_4^+	p_3^-	p_1^+	p_2^+	p_4^-	p_2^-	p_1^-	p_3^+	p_1^-	p_2^+	p_3^+	p_4^-	p_3^-	p_2^-	p_1^+
$[111]$	p_1^+	p_2^-	p_4^+	p_3^+	p_1^-	p_3^-	p_4^-	p_2^+	p_4^-	p_2^+	p_3^+	p_1^-	p_3^-	p_2^-	p_4^+
$[\bar{1}\bar{1}1]$	p_1^-	p_3^-	p_4^-	p_2^+	p_1^+	p_2^-	p_4^+	p_3^+	p_3^-	p_2^-	p_4^+	p_1^+	p_4^-	p_2^+	p_3^+
$[\bar{1}1\bar{1}]$	p_4^-	p_2^-	p_1^-	p_3^+	p_4^+	p_3^-	p_1^+	p_2^+	p_3^-	p_2^-	p_1^+	p_4^+	p_1^-	p_2^+	p_3^+
$[1\bar{1}\bar{1}]$	p_2^-	p_3^-	p_4^-	p_1^+	p_2^+	p_1^-	p_4^+	p_3^+	p_4^-	p_1^-	p_3^+	p_2^+	p_3^-	p_1^+	p_4^+
$[11\bar{1}]$	p_3^-	p_2^-	p_1^-	p_4^+	p_3^+	p_4^-	p_1^+	p_2^+	p_4^-	p_1^-	p_2^+	p_3^+	p_2^-	p_1^+	p_4^+

Figure 3.6 presents the resulting map of domain wall types and hence charging. With this specimen, the ratio of charged to uncharged domain walls is approximately 1:2.

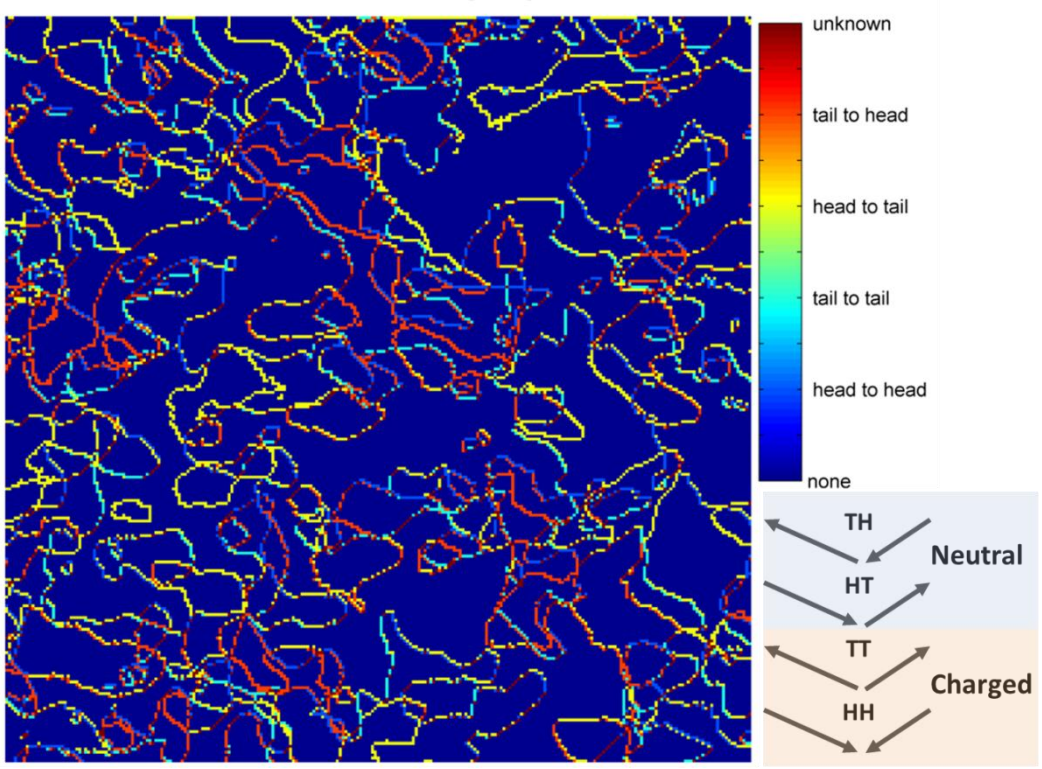

Figure 3.6 Map of domain boundary type/charging (charged: head to head, tail to tail; uncharged: head to tail, tail to head).

3.2 Comparison of $BiFeO_3$ 4, 2, and 1 domain Variants

In this section, the same strategy as that described above is applied to BFO samples with engineered 4, 2, and 1 domain variant configurations. These specimens are also epitaxially grown as described in Chapter 2, with 30 nm thickness, but were supplied by J. Ihlefeld from Penn State while in Dr. Schlom's lab (now at Cornell).

$BiFeO_3$ 4-domain variant

In the 4 domain variant BFO specimen, the out-of-plane and in-plane data at 0° and 90° is obtained in Figure 3.7 following the same procedure as described above. The combination of these images give rise to the domain polarization orientations. In the OP signal both at 0° and 90°, there is no contrast revealing that all domains are orientation

out of the surface ([111], [$\bar{1}$11], [$\bar{1}\bar{1}$1], or [1$\bar{1}$1]). IP data at 0° shows the color contrast indicating the front and backward polarization, while the 90° data indicates left or right facing domains as with Figures 3.2 and 3.3.

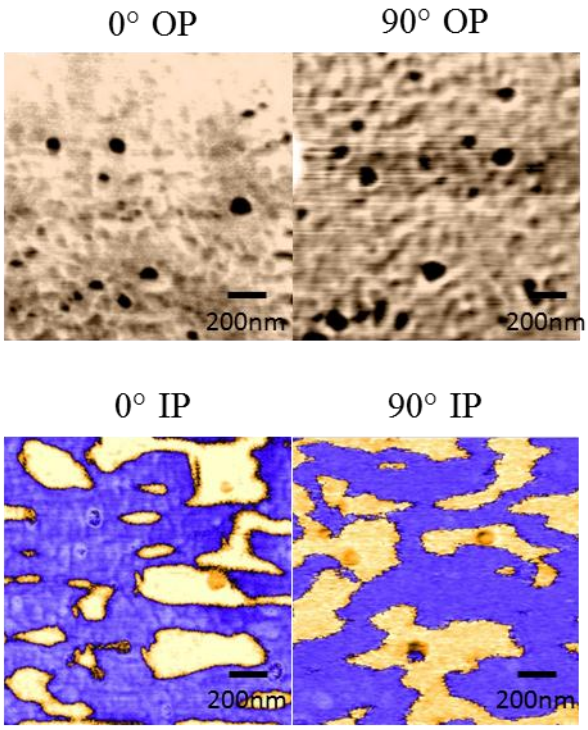

Figure 3.7 The OP and IP PFM images for 0° and 90° oriented scanning of the 4 domain variant sample.

Figure 3.7 further confirms the co-existence of all 4 domain variants for this specimen. However, unlike the previous sample which exhibited roughly equal proportions of all 8 possible polarization orientations, for this case only the outward polarizations of the 4 variants are present, Figure 3.8.

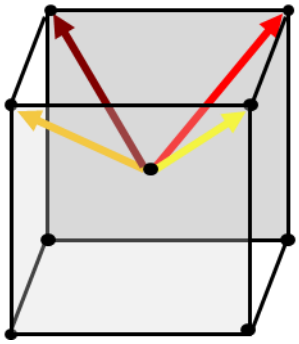

Figure 3.8 sketch of the possible orientations of the ferroelectric domains for the 4 domain variant BFO.

As before, the domain configuration can be fully mapped from such results, Figure 3.9(a). Once again, there are almost equal proportions of the possible domain types, with the exception that no domains whatsoever are oriented into the surface <hh-1>.

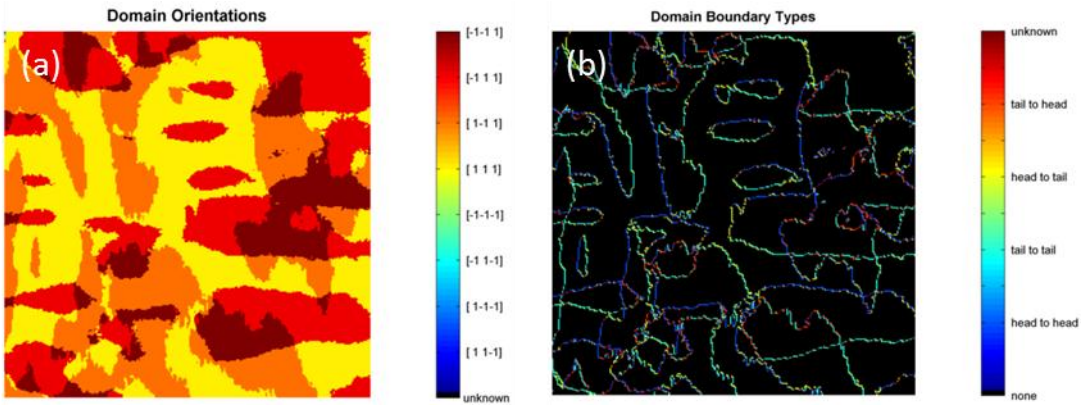

Figure 3.9 Domain orientation map (a), and domain boundary types (b) of the 4 domain variant $BiFeO_3$.

In addition, domain boundary angles and especially types can also be assessed, Figure 3.9(b). Considering this figure more carefully, the domain boundary type (and hence charging) can be seen to depend not just on the orientation of the neighboring domains, but also on the orientation of the domain walls. Considering any 1 domain, the type (color) of the domain wall changes when the domain boundary turns 90° (vertical to horizontal, or the opposite). The proportion of each type is basically equal though in every direction, since all possible IP orientations are present in this sample.

$BiFeO_3$ 2-domain variant

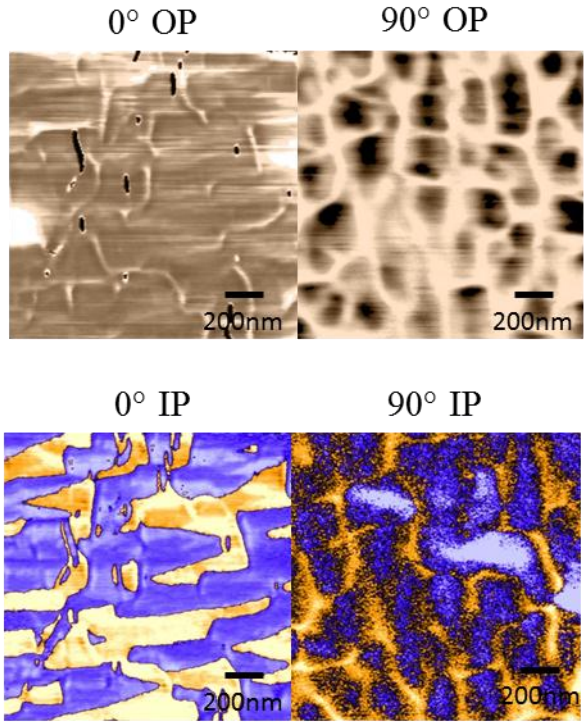

Figure 3.10 The OP and IP image at 0° and 90° of 4 domian variant sample.

For the 2 domain variant BFO specimen, the out-of-plane and in-plane data at 0° and 90° was once again obtained, Figure 3.10. As before, combining these results yield the domain polarization orientations present in the sample. As with the 4 domain variant sample described above, there is no strong color contrast in the OP signal both at 0° and 90°, revealing domains oriented only out of the plane ([111], [$\bar{1}$11], [$\bar{1}\bar{1}$1], or [1$\bar{1}$1]). The IP data at 0° indicates front and backward oriented pairs of polarizations, [$\bar{1}$11] or [1$\bar{1}$1], and [$\bar{1}$11] or [$\bar{1}\bar{1}$1]. The corresponding 90° IP data is absent of strong color contrast (simply weakly mimicking the OP contrast instead), so the pair of [$\bar{1}$11] and [1$\bar{1}$1]) cannot exist. With only a few small exceptions, this confirms that only 2 domain variants are represented ([$\bar{1}$11] and [$\bar{1}\bar{1}$1]) in this sample, Figure 3.11.

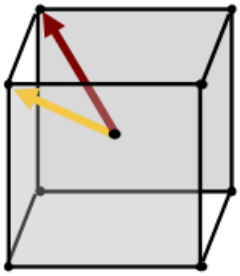

Figure 3.11 The possible ferroelectric orientations for the 2 domain variant BFO sample reduced to only 2 polarizations as expected.

Figure 3.12(a) presents the resulting domain orientation map for the 2 variant specimen, showing a majority of [$\bar{1}$11] and [$\bar{1}\bar{1}$1] polarizations. Figure 3.12(b), like Figure 3.9(b), gives an overview of the domain boundary distribution and types. As before, those domain boundary types depend on the orientation of the interface itself, but unlike the P4 variant sample, in this P2 variant the domain boundary types are much more uniform. In fact, all horizontally aligned domain walls are head to head or tail to tail, i.e. charged. All vertically aligned boundaries are head to tail or tail to head, i.e. uncharged. This may offer interesting possibilities for future device designs leveraging this orientation dependence.

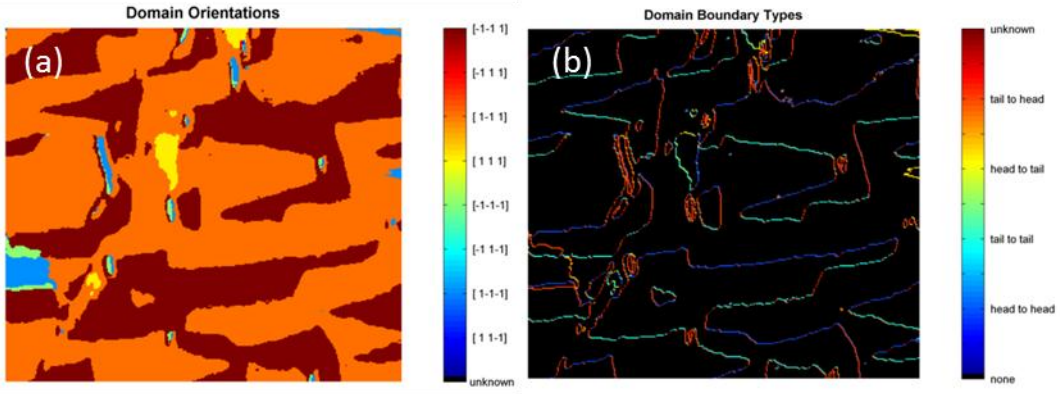

Figure 3.12 Domain orientation map (a) and domain boundary type (b) for the 2 domain variant $BiFeO_3$.

$BiFeO_3$ 1-domain variant

A single domain variant sample was also studied following the same procedure. All PFM images were featureless, so figures are not included for brevity. This confirms that this epitaxial sample was essentially a single domain without any domain boundaries present.

Domain Boundaries and Thermal Properties

In summary, the ferroelectric domain orientations were mapped for a set of 3 epitaxial films with distinct domain distributions (4 orientations, 2 orientations, or 1 orientation). In every case, all domains shared the same normal orientation, out of the plane of the sample. The distribution of domains in plane were distinct for the 3 specimens, however, including the domain wall density and type. Specifically, there were more domains present in a given area of the 4-domain film than the 2-domain sample, which equally exhibit more than the 1 domain sample. Quantitatively, the 4-variant BFO specimen exhibited 19.90 μm of domain boundary per μm^2, compared with 13.98 μm per μm^2 of the 2-variant specimen and essentially 0 boundaries for the 1-variant sample. The charged and uncharged proportions varied as well, but were not analyzed further. This may merit reconsidering if distinct properties (e.g. dielectric) are observed for the P2 specimen compared to the P4 sample, which Figure 3.12 would predict since horizontally vs. vertically aligned domain boundaries are predominantly charged or neutral, respectively. In any case, the thermal conductivity of these specimens was previously measured by Patrick Hopkins' group at the University of Virginia with time domain thermoreflectance. There is a clear trend in the effective thermal conductivities of the $BiFeO_3$ and the number of domain variants. An increase in the number of domain variants and, particularly, density of domain walls in the film leads to a decrease in thermal

conductivity, in figure 3.13. This can be ascribed as phonons scattering in the domain boundaries and creating a temperature gradient though the domain walls. When more domain boundaries are present in the $BiFeO_3$, increased phonon scattering occurs leading to lower thermal conductivities. This effect is similar to the influence of grain boundaries on thermal conductivity, exemplified by the overlain results for polycrystalline $SrTiO_3$. These results therefore show, for the first time, that domain walls can act as scattering sites which impede thermal conductivity. Thermal conductance of $SrTiO_3$ is also measured here for comparison as a bulk material.

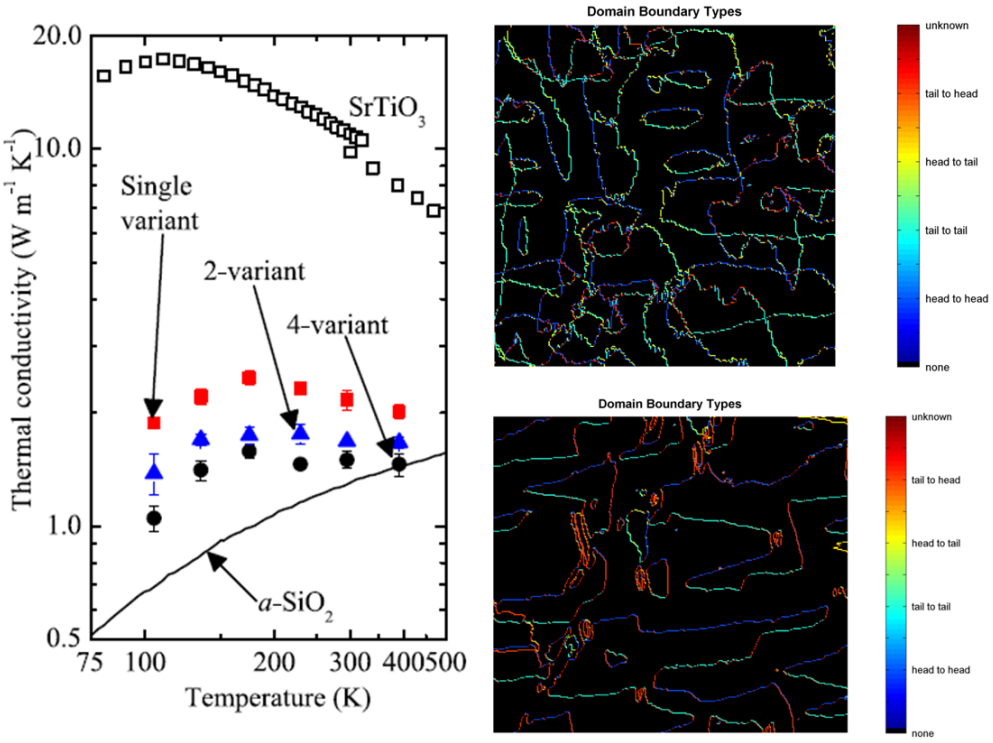

Figure 3.13 Thermal conductivities measured by collaborators for 5 specimen types, including all 3 BFO specimens investigated in this study (left), along with a summary of the domain boundary densities and types (right) for the 4 (top) and 2 (base) domain variants.

Both out of plane and in plane PFM imaging has been performed with specimens oriented at 0° and 90°, allowing complete domain maps to be acquired for epitaxial (001) $BiFeO_3$ thin films or any other ferroelectric with <111> polarization directions. An automated

procedure was further developed to statistically analyze the domain boundary density in the image, the domain boundary rotation angles, the proportion and location of charged or neutral domain walls, etc. This procedure was then followed for 3 BFO specimens engineered to exhibit specific domain configurations, specifically 4, 2, and 1 domain variants. The results indicated an increase in the domain wall density with the number of domain variants. Thermal conductivity measurements on the same specimens indicate an inverse trend in performance with domain variants. These results show, for the first time, that domain wall boundaries influence thermal conductivity by scattering phonons similar to grain boundaries, and therefore higher densities of domain walls cause lower thermal conductivity.

3.3 References

1. Joseph Desmarais, J.F.I., Tassilo Heeg, Jürgen Schubert, Darrell G. Schlom, *Mapping and statistics of ferroelectric domain boundary angles and types.* Applied Physics Letters, 2011. **99**(16).

Chapter 4. Domain Dynamics

Ferroelectric domain dynamics have also been investigated. Significant progress in developing methods for such measurements were recently published by previous group members. Here, the question is asked whether domain growth is influenced by crystallographic orientation and/or imaging artifacts such as the AFM scanning directions.

4.1 Domain Patterning

Domain growth has been investigated by monitoring switching with PFM for Eight pre-poled domain configurations. These are based on 4 distinct geometries of pre-poled domains: 0.5 μm width x 1 μm length rectangular patterns; 1 μm width x 1 μm square patterns; 0.5 μm width x 2 μm lengths; 1 μm width x 2 μm lengths. Those four types of pre-poled initial domains were then aligned at two distinct angles for scanning: 45° and 90°. Domain wall motion was then followed and the velocity calculated for domains moving parallel to the scan axis, perpendicular to it, and/or at 45 degrees. In every case growth was investigated based on consecutive 2 μm by 2 μm PFM images, acquired with simultaneously applied AC and DC biasing in order to gradually grow the pre-nucleated domain structures. Figure 4.1 presents examples of several of the pre-poled patterns and pattern orientations with respect to the scan axes, which are along Cartesian directions where the fast scan direction is lateral (x) and the slow scan rate is vertical (y).

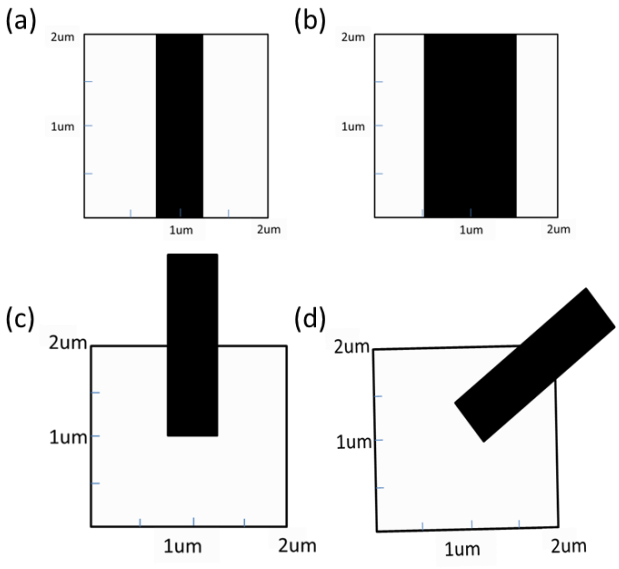

Figure 4.1 Geometries of the initial domain configuration in theory, (a) 2 μm in length x 1 μm in width; (b) 2 μm in length x 0.5 μm in width; (c) 1 μm in length x 0.5 μm in width; (d) 1μm in length x 0.5 μm in width at 45º.

Technically, the first step in the measurement is to backpole an entire region by scanning with a large negative DC bias in order to provide a uniformly poled area for domain switching studies. The initial scan size is 3μm by 3μm, larger than the eventual results of interest to accommodate thermal drift during experiments. Other parameters include a scan rate of 4 Hz and a 0.8 V contact mode set point. The lock-in amplifier is set to no filter.

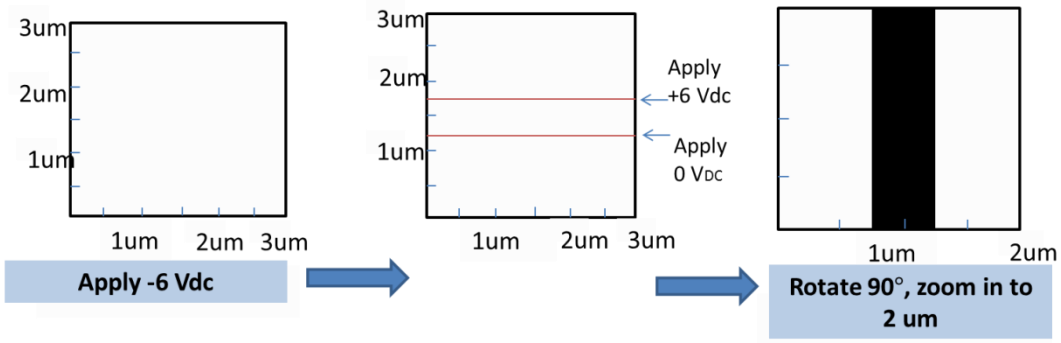

Figure 4.2 The process of pre-poling domain.

In the second step, positive DC voltages are selectively applied while the tip rasters the surface again, but only in certain areas. For example, as is shown in Figure 4.2, the central positively poled region extends 0.5 (or 1, or 2) μm. After rotating the scanning direction by 90°, the prepoled pattern is then reoriented. It is now reimaged with PFM in the AC mode only, using a sub-coercive field to confirm but not manipulate the initial poling. Specifically, we applied a 8 V_{PP} Amplitude at a 1700 kHz contact resonance, identified by the Resser program as described in Chapter 2. This results in PFM phase images similar to the sketch at right, though domain wall edges are seldom perfect as discussed later.

Figure 4.3 presents PFM phase contrast for 4 specific initial domain patterns aligned at 0° with respect to the scanning direction. This includes imaging near the center of the rectangular domain patterns (top) for both narrow (left) and wider (right) prepoled regions, as well as images at the end of those same narrow and wide domains (base). Switching near the ends of the pre-poled boxes will be particularly revealing as it can provide domain growth velocities parallel, and perpendicular, to the scanning direction.

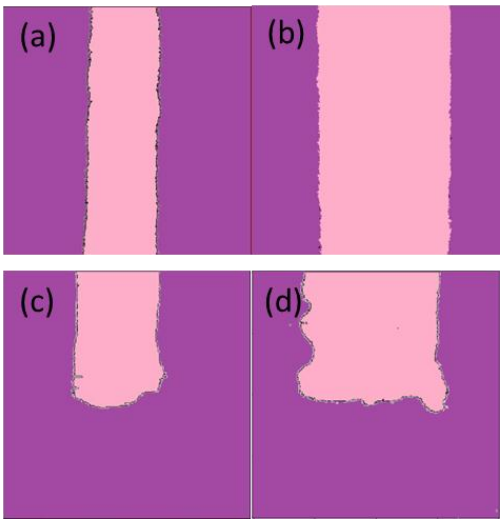

Figure 4.3 PFM images of (a) the initial poled domain in geometry of 2 μm in length x 0.5 μm in width; (b) the initial poled domain in geometry of 2 μm in length x 1 μm in width; (c) the initial poled domain in geometry of 1 μm in length x 0.5 μm in width; (d) the initial poled domain in geometry of 1 μm in length x 1 μm in width.

4.2 Switching Movies

Domain switching movies are acquired by superimposing a 1.7~1.8 V DC offset during consecutive PFM imaging of a prepoled box and its vicinity. The results can be divided into three main categories: 1) the impact of the initial domain sizes on the velocity of the domain wall movement; 2) comparisons of domain growth parallel and perpendicular to the fast scan (x) direction; and 3) domain growth at 45°. By defining domain growth at 45º, We first scan at -45º when poling the initial domain configuration; the next step is to apply AC and DC voltage simultaneously to make the domain switching at a scan angle of 45º. In this case, based on the AFM image, it still looks the same as previous ones, whereas the initial domain was an triangle box along the diagonal actually. This process allow us to study the domain growth along the <110> directions. All switching movies are acquired with 10 Hz line rates, representing moderate speed SPM imaging.

As an example, Figure 4.4 presents a montage of consecutive PFM images during switching of a 0.5 µm wide pre-poled box. It was expected that the domain wall would grow horizontally both to the left [$\bar{1}$00] and to the right [100]. Additional domain nucleation and even domain coalescence naturally occurred in the vicinity, which masked the late stage growth dynamics of the pre-poled region into the surrounding film. The initial stages (Frames 1-7), however, still provide a means to assess lateral domain wall motion for a single pre-poled structure.

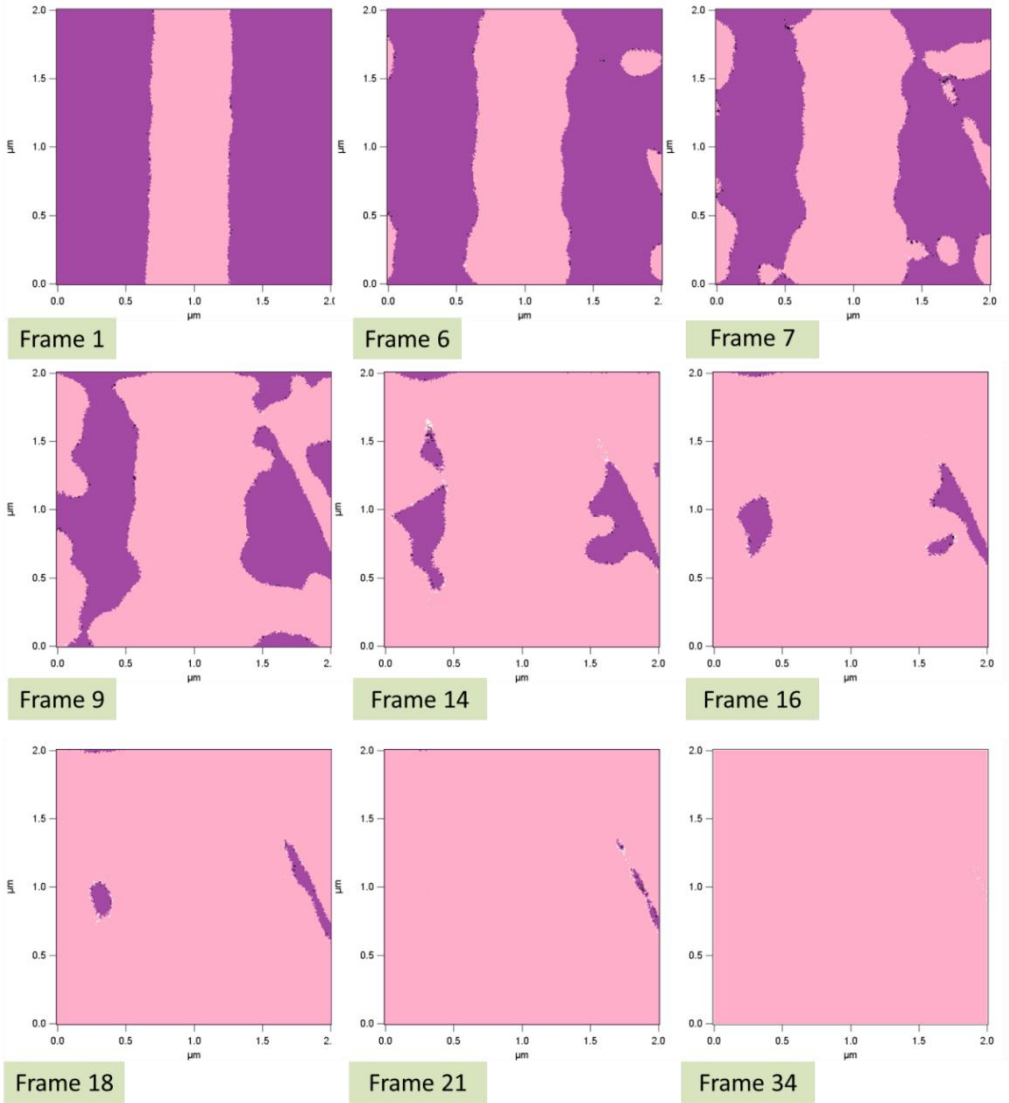

Figure 4.4 The switching process of in the case of 2 µm length x 0.5 µm in width.

The number of particles in each frame can be quantified in Figure 4.5. Lots of small of small particles tend to grow after frame 5 due to the voltage comparing with the relatively less nucleation at the very first stage. Then the independent domains tend to extend and form into bigger sizes with the particles numbers decreasing dramatically.

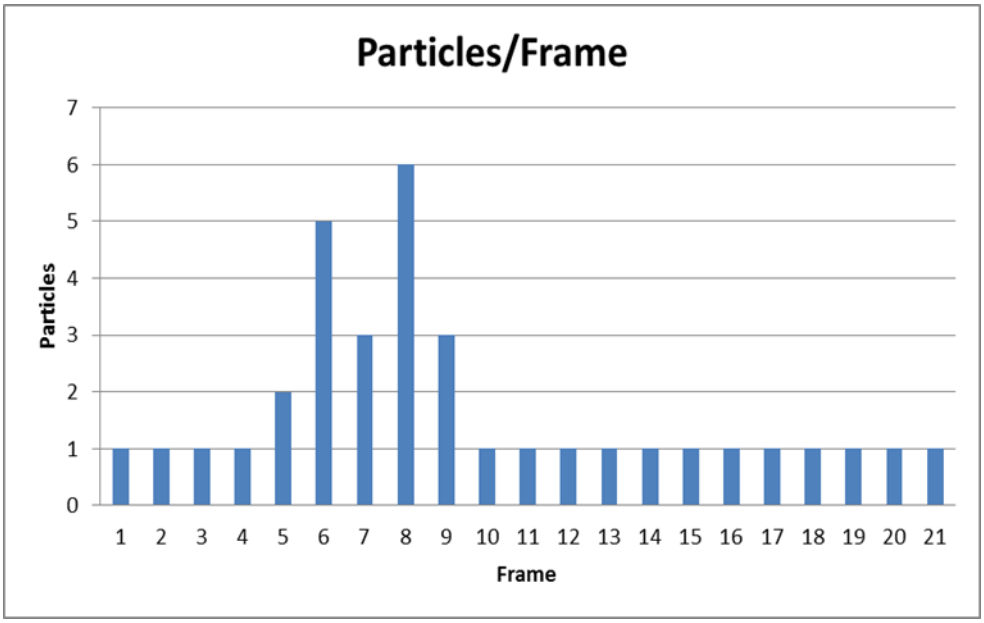

Figure 4.5 Sum of the particles appear during each frame for the 2μm x 0.5μm domain in 90°.

Figure 4.6 presents similar looking switching results, where growth of a prepoled region alone can again be recorded over several frames before coalescence with nearby nucleated and growing domains. In this case, though, the pre-poled box was initially oriented at -45° (along a <110> instead of a <100> direction), while scanning was performed at 45° (along a transverse <110> direction). As a result, the scan direction has been changed, but the fast scan axis is still perpendicular to the prepoled structure. Therefore, the scanning direction itself is found to be irrelevant to the results, confirming that this possible artifact in switching movies is negligible.

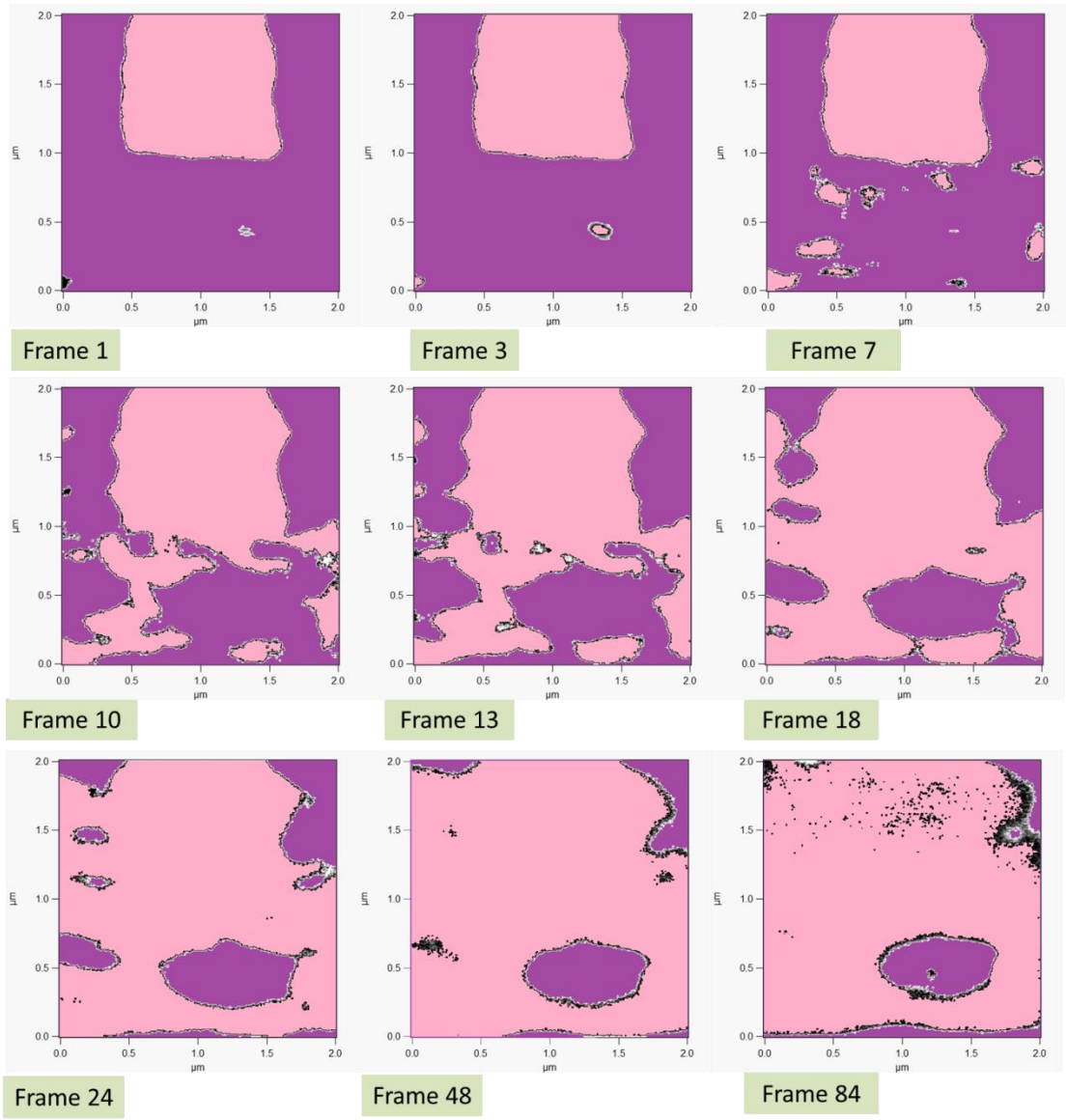

Figure 4.6 Switching process of the short 1 µm x 1µm domain box scanning at 45°.

Preferential domain growth along, or perpendicular, to the AFM fast scanning direction is another possible experimental artifact that must be explored. The switching movie in Figure 4.6 was acquired at the end of a prepoled rectangle, enabling exactly such measurements where growth can be visualized parallel and perpendicular to the path of the tip. Growth clearly occurs in both of these horizontal and vertical directions, respectively, except for a region at the base of the images which seemingly cannot

switch. This anomaly, though, is not surprising since simultaneous AFM topography reveals this location to have a protruding contaminant particle, severely diminishing the locally applied fields and hence perturbing or even preventing switching at this site.

4.3 Growth Velocity Analysis

Given the polarizations and voltages employed, during the switching process the light shaded central region (poled by a positively biased tip) expands towards the edges of the image at the expense of the dark colored surroundings (negatively poled). To quantify growth velocities, enough images were acquired that an automated procedure was necessarily developed. Briefly, commercial image analysis software (Image J) is used to convert the phase signal for all image pixels to binary contrast. These are then analyzed directly in ImageJ, or exported for analysis as simple spreadsheets or for more sophisticated calculations with Matlab.

Previous efforts either assumed uniform radial domain growth, or uniform lateral domain expansion across a given area of interest (or entire image). In that case, the average contrast in this region (or area) could simply be automatically calculated as a function of the image frame (poling time) in order to calculate the domain wall velocity. For example, Figure 4.7 presents the switched area per frame beginning with approximately 55% of the image area prepoled. Eventually, the switched area fraction approaches 98%, with most switching occurring between frames 5-10. Careful inspection of the switching movies, though, shows that this approach is insufficient since additional domains tend to nucleate and hence interfere with such full area averaging methods.

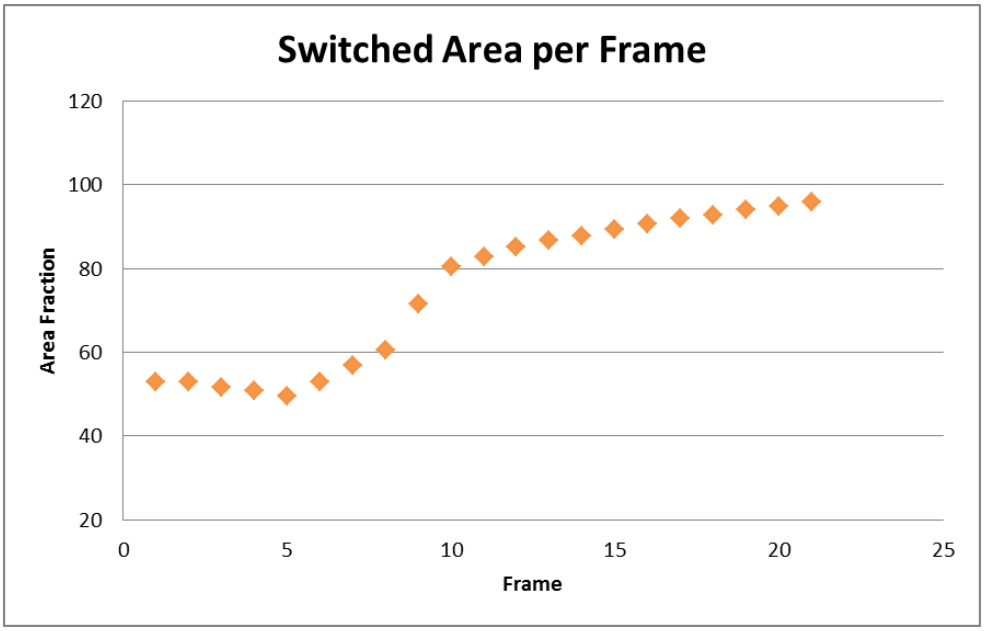

Figure 4.7 Calculations of the switched area fraction (here for the 2µm x 0.5µm domain imaged at 90°) can be used to calculate growth rates for uniform growth and single domains, but are not specific enough for polydomain formation as observed here.

Instead, the average domain wall position for every single image in a switching movie is determined based on cross sections of the image contrast along certain axes. Comparing the domain wall pixel position from one image frame to the next, and knowing the image dimensions, finally yields the traversed distance, Equation 18. This is converted to a domain wall velocity based on the poling time per pixel (typically 5 usec/frame), Equation 19. Domain growth velocities in any given direction can therefore be determined and related to sample composition, defects, adjacent domains, etc.

$$\boldsymbol{distance}|_{\boldsymbol{frame}}=\frac{\boldsymbol{Image\ Size}_{\boldsymbol{in\ um}}}{\boldsymbol{Image\ Size}_{\boldsymbol{in\ pixels}}} * (\boldsymbol{position}_{\boldsymbol{i}} - \boldsymbol{position}_{\boldsymbol{0}})|_{\boldsymbol{pixels}} \qquad (18)$$

$$\boldsymbol{velocity} = \frac{\boldsymbol{distance}}{\boldsymbol{frames} * \boldsymbol{5\ \mu s\ poling}/_{\boldsymbol{frame}}} \qquad (19)$$

Figure 4.8 exemplifies this approach, where the stepwise growth is clear based on the differently shaded hypothetical 'image' frames. In fact, though, the domains do not

always grow uniformly as sketched below, which is clearly evidenced in the previous PFM image sequences. Therefore, instead of measuring the domain position along a single line, the contrast perpendicular to that line is thus averaged (notably only those pixels adjacent to an expending domain were considered).

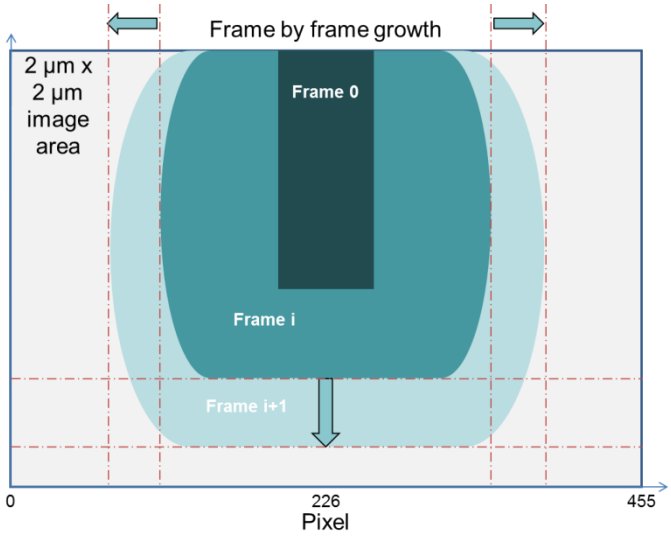

Figure 4.8 Sketch of the measurement of the switching domain in each frame along both vertical and horizontal way.

As an example, Figure 4.9 presents the vertically averaged contrast along a horizontal line that traverses a vertically aligned domain, exactly as depicted in the previous results and sketch. For successive image frames, the central domain expands laterally. The domain edges are then defined based on the location where 75% of the pixels have switched, i.e. where the average contrast reaches 192 (75% of the maximum value of 256 for the 8 bit images that are typically considered). For differently oriented domain walls or growth, the same approach is followed after adjusting the cross-sectional directions and their transverse averaging segments.

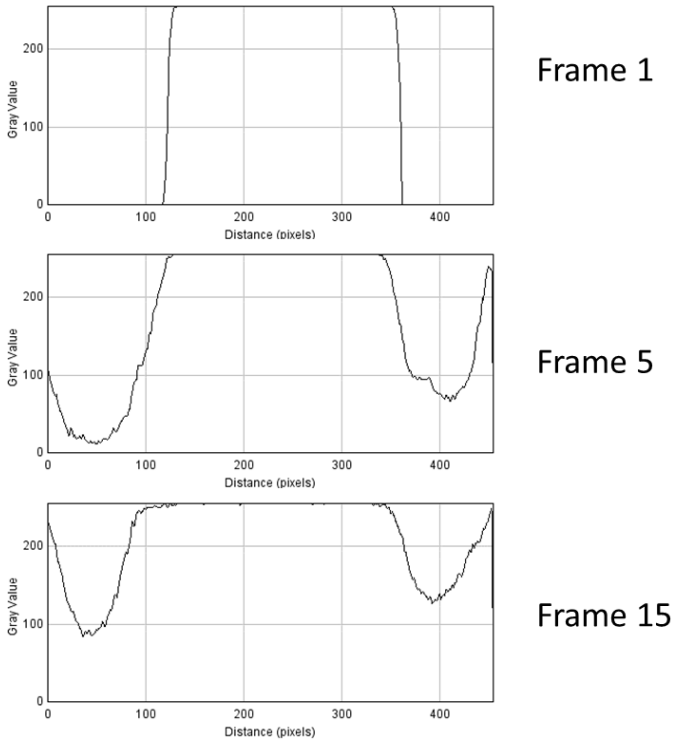

Figure 4.9 Average cross sections for an expanding central pre-poled domain with initial dimensions of 2µm x 1µm, as well as domains eventually nucleating and growing in from the image edges.

Taking 2µm x 0.5µm pre-poled domains written and read along <110> directions as example, the left, right, and combined domain wall edge have been monitored as a function of time, figure 4.11.

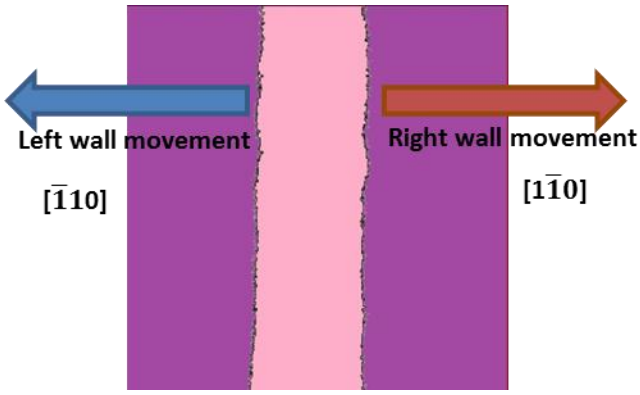

Figure 4.10 Sketch of the crystallographic directions in domain wall movement of the 2µm length domain configuration.

Plotting the results indicates that the left domain wall moves further left, and the right wall moves right, with poling, i.e. domain growth occurs in both directions. This is hardly surprising, though, the growth rate unexpectedly appears to be different in these opposing directions. This is likely due to image drift during the measurements, though, which can be accommodated either by drift correction (based on tracking features in topography), or in this case even more easily by simply monitoring the expanding domain width. The prepoled domain essentially grows linearly after approximately 10 imaging frames.

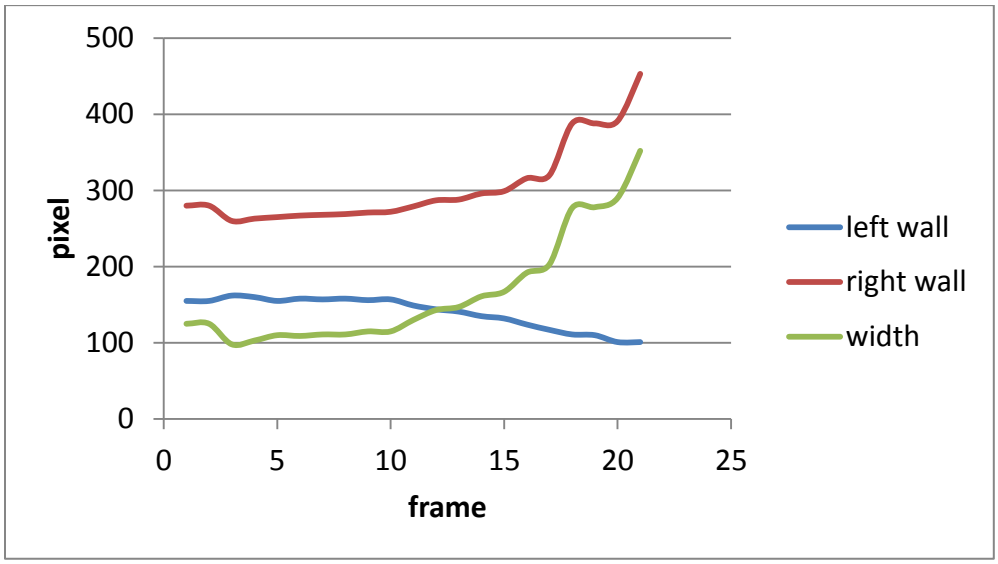

Figure 4.11 The pre-poled domain walls for the 2µmx0.5µm-45° condition grow in opposite directions with increasing poling frames (poling time); monitoring the width corrects for image drift that occurred for this particular switching movie (predominantly towards the right).

Similar measurements have been prepared, but to monitor <110> oriented domain growth instead of the presumably crystallographically preferred <100> growth. Again the domain wall expands both to the left [$\bar{1}$10] and the right [1$\bar{1}$0]. Figure 4.12 presents the corresponding stepwise domain expansion.

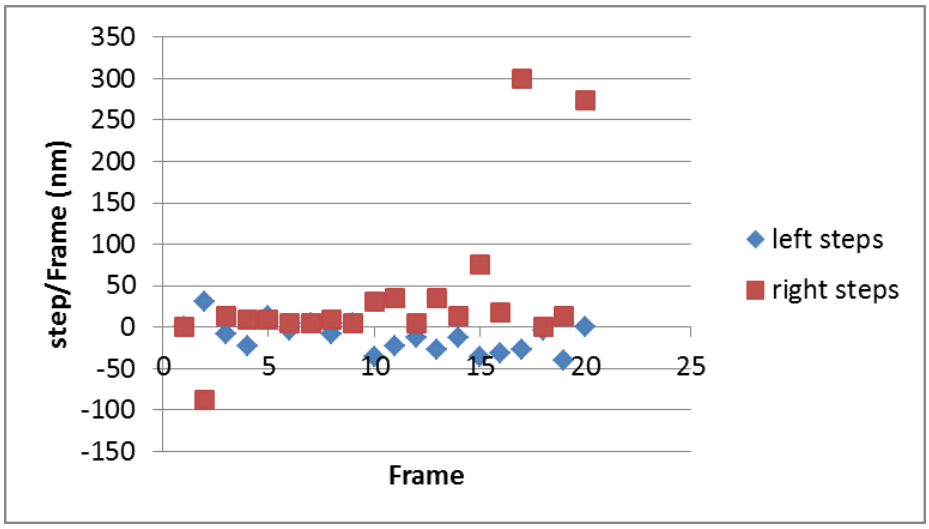

Figure 4.12 This shows each step of the left [$\bar{1}10$] and right [$1\bar{1}0$] domain wall movement with poling frame (time) for the 2µmx0.5µm-45°.

Figure 4.13 presents the domain wall velocities from the results of such figures, as well as similar data except for different pre-poled feature dimensions as well as orientations (pre-patterning and growth). For every case, the domain wall velocity is substantially faster for initially wider domains. This could be a kind of experimental artifact, e.g. resulting from slightly different biasing used during acquisition of the switching movie. Other explanations intrinsic to the thin films are also possible, a point that is discussed in further detail later in this chapter.

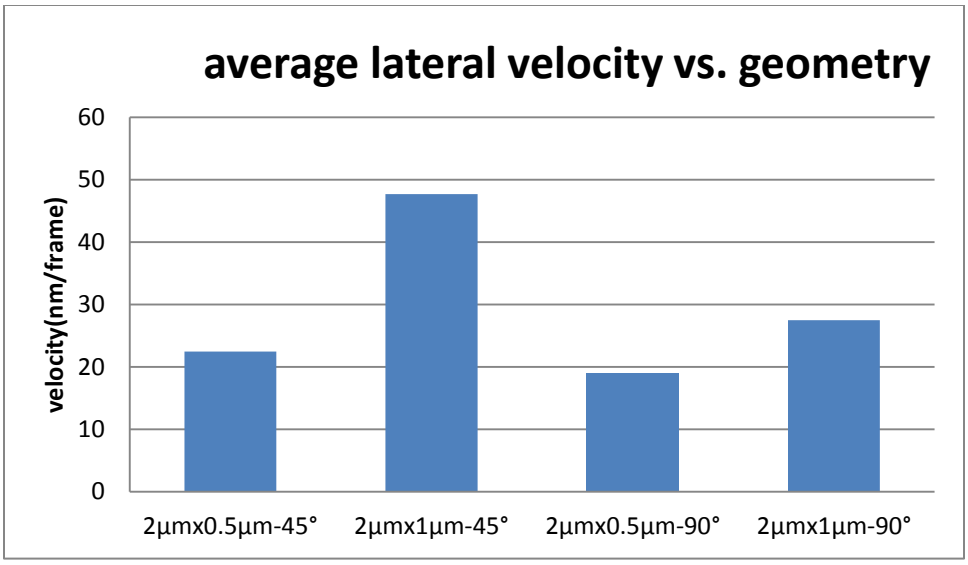

Figure 4.13 Velocities and direction relations.

As previously introduced, domain growth has separately been monitored in perpendicular directions during expansion of a single domain. Taking the 1µmx0.5µm-90° condition as an example, domain growth is monitored along [100] and [-100], and compared to [010] growth for a prepoled domain and switching movie configured as shown in Figure 4.14.

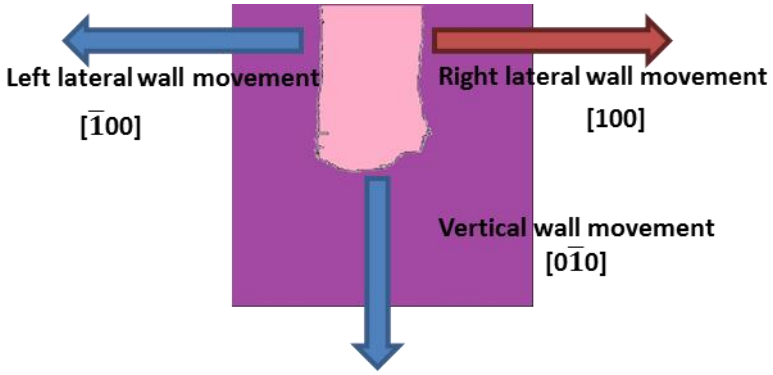

Figure 4.14 Sketch for the domain movement direction of 1µmx0.5µm-90°.

The results for [100] and [-100] growth again reveal moderate asymmetry for left vs right moving domain walls. Therefore, the expanding domain width is a more representative measure of domain wall velocity when available.

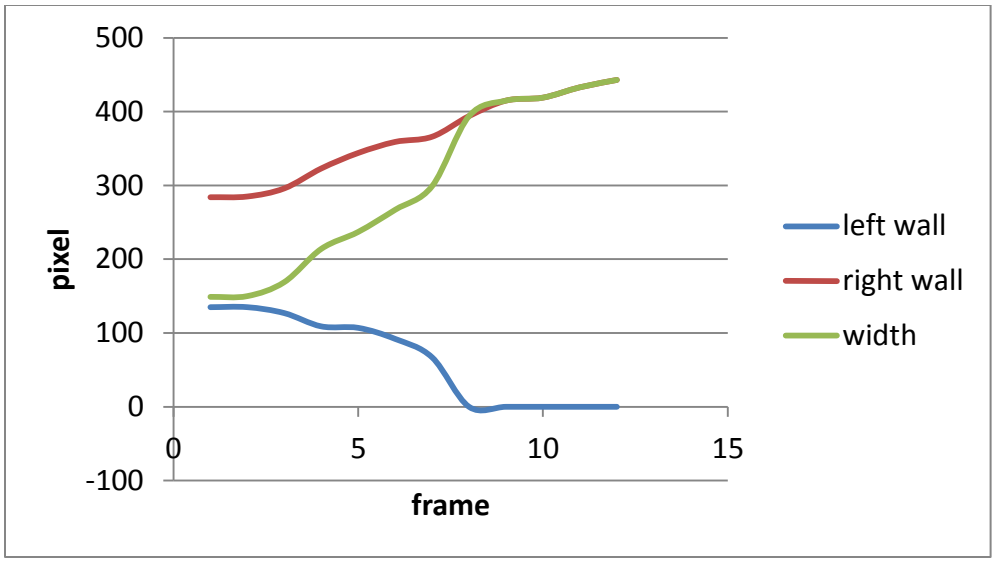

Figure 4.15 Blue and red line Show how the right wall and left wall moves in each direction in term of pixels vs. time, the green line indicates the width between them during time.

Figure 4.16 presents results in the transverse direction, $[0\bar{1}0]$. Unlike the horizontal domain growth, vertically the domain appears stable until it abruptly jumps. Once again, however, inspection of the switching movie reveals that this is likely due to the unlucky presence of a contamination particle, skewing the switching fields and hence the local switching dynamics. Local pinning due to film defects may also interfere, especially since the domain wall width being considered for vertical growth is relatively small compared to the domain wall length being averaged for lateral motion.

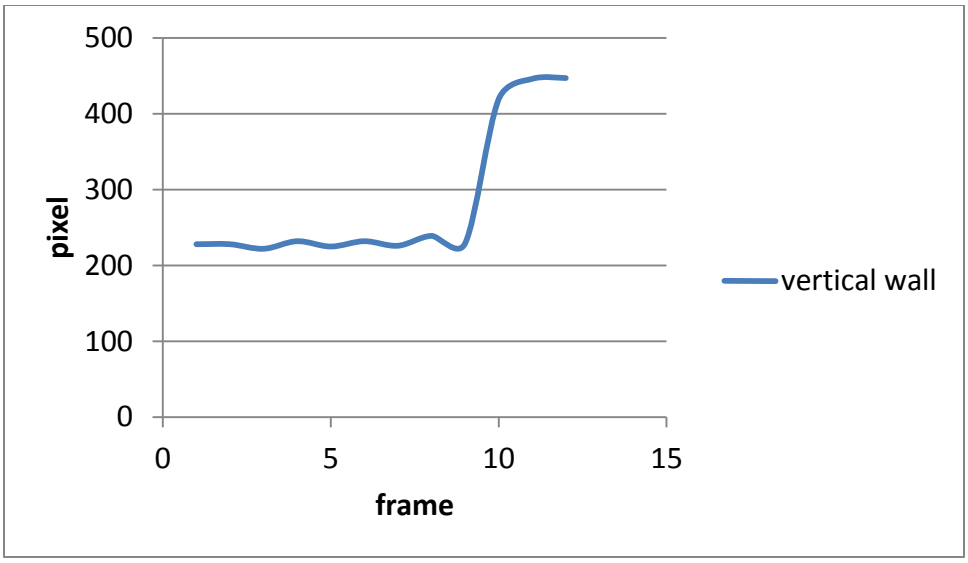

Figure 4.16 Plot of the vertical [100] domain wall position with poling time.

The switching movies presented early in the chapter clearly exhibit such heterogeneous nucleation and growth on approximately the ½ micron scale. Therefore domain growth averaged along only 1 um of interface (or half that) is expected to be far more susceptible to heterogeneous effects than the several microns of domain length averaged across for the lateral growth statistics.

4.4 Results and Discussion

Figure 4.17 considers the velocity size dependence more carefully than Figure 4.13, both for the horizontal [100] direction perpendicular to the long edge of the prepoled domain pattern (i.e. their sides), and also for the harder to measure vertical [$0\bar{1}0$] direction perpendicular to the short edge (i.e. the end) of the prepoled domains. Unlike the anomalous case of Figure 4.16 where this vertical domain growth was impeded by some kind of defect (intrinsic or extrinsic), all other switching movies in fact exhibited an enhanced domain wall velocity perpendicular to the short edge of the pre-poled domain

pattern. This is exactly the opposite of what would be anticipated if the result is due to AFM based scanning artifacts, where enhanced speeds would be expected along the fast scanning axis instead of perpendicular to it.

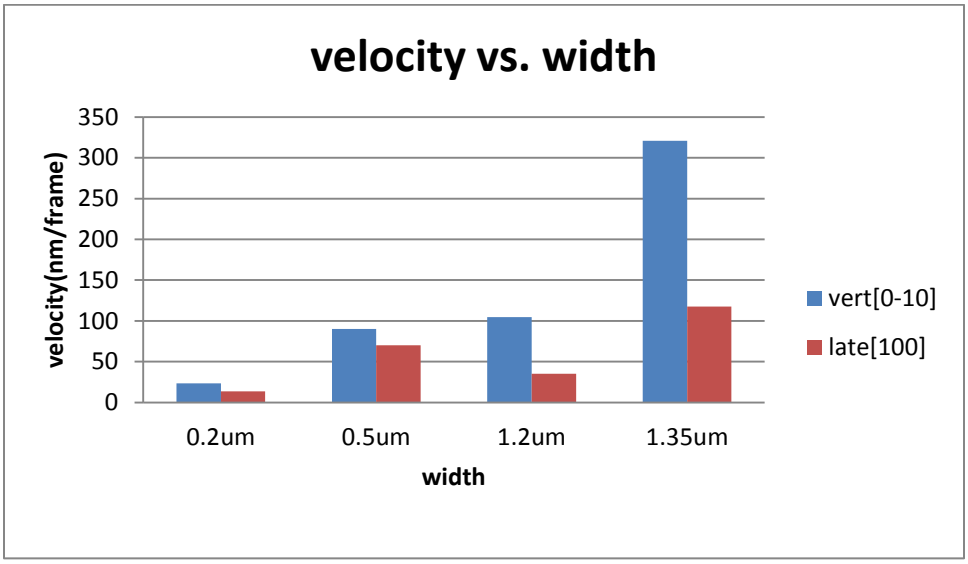

Figure 4.17 Orientation vs. width in the 1µm-length-90° with different widths.

Again comparing Figure 4.13 with 4.17, the trend of increasing velocity with widening initial domain pattern now convincingly occurs, and for both domain wall alignments. In fact, an order of magnitude enhancement is observed for the growth velocity over nearly an order of magnitude change in initial domain width.

Finally, the relative ratio of vertical to horizontal velocities have been calculated for several experimental conditions. This includes domain growth along unit cell faces (<100>), as well as at 45° to these crystallographic directions (i.e. along <110>).

As seen in Figure 4.18, again the wider (1µm vs. 0.5 µm) domains behave anomalously, with substantially faster growth normal to the short edge (vertically) than the long one (horizontally, with the fast AFM scan axis). This is true for both crystallographically aligned domain patterns <100>, and those canted by 45° <1-10>.

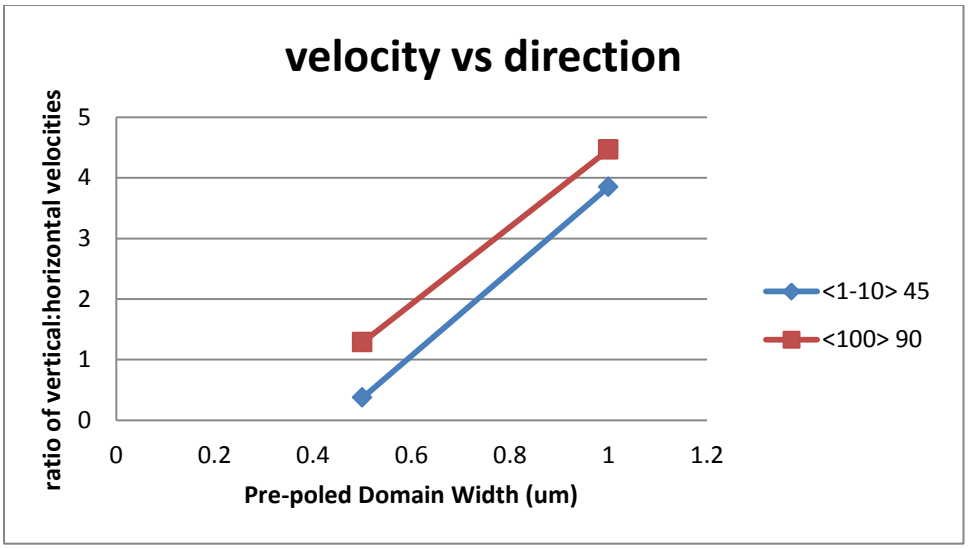

Figure 4.18 velocity ratios with different domain sizes.

These effects prove that the poling process itself can influence switching dynamics. Such behavior has in fact been observed before, by group-mate Nicholas A. Polomoff as evidenced in Figure 4.19. This figure identifies more than 100 indeividual domains which nucleated during switching movies acquired similar to the procedure followed throughout the current work, only small box-shaped patterns were pre-poled instead of isolated rectangular structures. Domain nucleation and growth is very clearly inhibited in the immediate vicinity of the pre-poled patterns, extending up to 250-500 nm away from the initial domain boundary. This also resulted in distinct growth behavior for the pre-poled domains, not shown, which was enhanced as compared to those domains nucleating independently. This has similarly been convincingly proven in the present work, but for a range of growth directions, initial domain geometries, etc. The most likely explanation is charge accumulation or depletion at and/or adjacent to the pre-poled patterns.

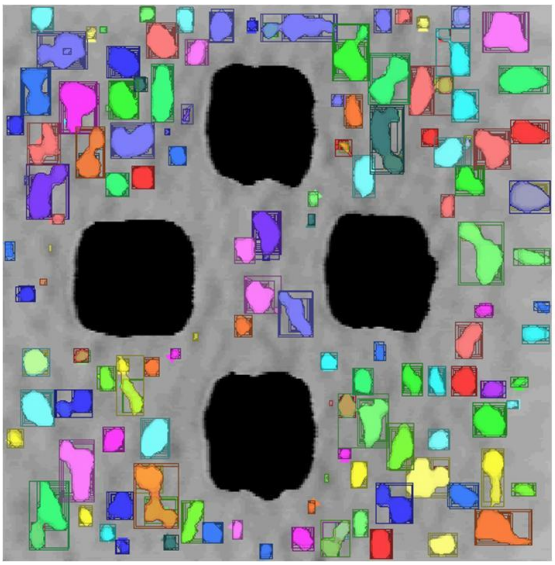

Figure 4.19 Domain nucleation with pre-existence poled pattern.

4.5 Conclusions

Ferroelectric domain growth has been thoroughly investigated as a function of pre-poled domain sizes, crystallographic orientation, and pattern alignment. Possible experimental artifacts causing enhanced domain growth along the fast scanning AFM axis are disproven. In fact, domain velocities are instead found to be consistently higher normal to the fast-scan axis, regardless of the crystallographic alignment of the domain boundaries. More interestingly, larger initial poled structures convincingly grow faster than small patterns. The question of why these pre-poled domain patterns exhibit such enhanced growth is still unanswered, but this may have interesting self-limiting implications for ultimate switching velocities as ferroelectric device dimensions continue to shrink.

4.6 References

1. D. Schrade, R.M., D. Gross, T. Utschig, V.Ya. Shur, D.C. Lupascu, *Interaction of domain walls with defects in ferroelectric materials.* Mechanics of Materials, 2006. **39**.

Chapter 5. Conclusions and Future Work

Chapter 1 provided a general background about ferroelectric domains, their significance, and their detection and mapping with various experimental techniques. Chapter 2 presented details for how piezo force microscopy (PFM) is specifically used in the Nano Measurement Labs to map ferroelectric domain orientations. Chapter 3 described experiments and results for $BiFeO_3$ thin films which revealed the map of domain polarization orientations, domain wall angles and distribution as well as the thermal conductivities of $BiFeO_3$ with different domain wall densities. Finally, Chapter 4 investigated domain switching dynamics in PZT with in-situ poling and PFM. These results proved that domain growth velocities are not related to the AFM scanning direction, and instead are connected to crystallographic orientations as expected. Surprisingly, though, domain growth was also found to depend on the initial poling parameters, suggesting charge accumulation or depletion processes under some poling conditions which can enhance switching in adjacent regions.

Building on these results suggests several directions for future work. In terms of PZT switching dynamics, the previous efforts were based on the growth of single domains. It would be interesting to extend this concept to interactions between multiple domains, and especially for domains with particular domain wall directions with respect to the underlying crystallographic symmetry. For instance, two rectangles crossing at 45 degrees, with domain walls along <100> and <110> directions, could next be considered

for direct comparison of relative velocities. This will also provide insight into the interplay between adjacent domain walls as a function of their approach angles. Instead of monitoring such domain growth under external biasing, thermally induced domain relaxation could equivalently be studied, again as a function of domain wall orientation with respect to crystallographic symmetry, intersecting domain wall angles, etc. Conductivity mapping is also an interesting extension of the current work. Employing the voltage lithography skills I have acquired, conducting channels could be fabricated for LAO ultra-thin films on STO. The LAO/STO interface exhibits a bistable metal-insulator transition, which can be tuned by applied biases at room temperature. By biasing an AFM tip as it is scanned in a single line from one electrode to another in contact mode, the tip will generate the necessary electric field to enable local conductivity transitions. Nanowires and nano islands can thus be written, and as it happens also erased by opposite voltages akin to ferroelectric domain patterning, but with conductivity control instead of simple polarization and/or piezoresponse. Employing conductive AFM instead of PFM, current images can then map the resulting conductive pathways, and their evolution with time, voltage, temperature, etc. This ability to reversibly pattern conductive and insulating regions at the nano-scale provides an exciting new area of research with many fundamental and practical implications.